Propagation of a fluid-driven fracture with fracture length dependent apparent toughness

Dong Liu[a], Brice Lecampion[a,*], Dmitry I. Garagash[b]

[a]Geo-Energy Laboratory- Gaznat chair on Geo-Energy, Ecole Polytechnique Fédérale de Lausanne, ENAC-IIC-GEL-EPFL, Station 18, CH-1015, Switzerland
[b]Department of Civil and Resource Engineering, Dalhousie University, NS, Canada

Abstract

We investigate the growth of a hydraulic fracture assuming a power-law dependence of material toughness with fracture length for plane strain and radial geometries. Such a toughness fracture length dependence models in a simple manner a toughening mechanism for rocks. We develop an efficient numerical method for the hydraulic fracture growth problem combining Gauss-Chebyshev quadrature and Barycentric Lagrange interpolation techniques. Scaling and numerical results demonstrate that the transition from the viscosity to the toughness dominated regime occurs earlier. The toughness dominated regime always governs growth at large time for both geometries. In all cases, larger net pressure and shorter length are obtained. The solution is very well approximated by the existing constant toughness solutions using the instantaneous value of toughness. If the apparent fracture toughness saturates beyond a given length scale, the solution transitions back to the constant toughness solutions.

Keywords: Hydraulic fracture, Fluid-solid coupling, Apparent toughness, Gauss-Chebyshev methods

1. Introduction

The propagation of a hydraulic fracture (HF) in an impermeable elastic solid is relatively well understood, with theoretical predictions matching laboratory scale experiments in model material (e.g. PMMA, glass, cement) at least for simple planar fracture geometries [1, 2, 3]. In particular,

---

*Corresponding author: brice.lecampion@epfl.ch

the ratio between the energy dissipated in the creation of fracture surfaces (fracture energy) versus the energy dissipated in fluid flow [4, 5] governs HF growth, leading to either toughness dominated or viscosity dominated propagation.

Despite the relatively good agreement of hydraulic fracture mechanics predictions with laboratory experiments performed in brittle/fine-grained materials, deviations from theoretical predictions have been reported in field observations and micro-HF treatments in vertical wells [6, 7, 8, 9]. Apart from a possible increase of fracture energy[1] in the field compared to the laboratory scale, such deviations, in particular a larger propagation net pressure (the difference between the fluid pressure and the confining stress) might also be explained by other factors such as the additional frictional losses associated with near well-bore fracture tortuosity [10, 11]. In any case, these field observations indicate a higher energy demand for larger scale fractures, and hint to further study of the HF growth in quasi-brittle materials.

A process zone develops around the fracture tip in quasi-brittle materials, where non-elastic processes such as micro-cracking and plastic deformations are present. The size of the process zone acts as a good indicator of the apparent fracture energy. Rubin [12] has investigated theoretically a propagating HF under high confining stress adopting a cohesive zone model. He argues that the tip cavity (fluid lag) generated by viscous fluid flow grows with the fracture and results in an increase of the process zone size and energy consumption via the perturbation of the near-tip stress field. Numerical studies [13, 14, 15, 16, 17] accounting for plastic dissipation of a propagating hydraulic fracture have shown a higher net pressure and wider inlet opening, implying an increase of the apparent fracture toughness[2] up to more than one order of magnitude [13, 15]. Hashida et al. [18] have reported hydraulic fracturing experiments on Iidate granite spanning fracture radius between a few millimeters up to 20 centimeters (on specimen size up to metric scale). These tests clearly show an increase of the toughness with fracture radius following approximately a power law (see Fig. 1-right). In plaster blocks, Van Dam et al. [19] have reported a development of the fracture tip bluntness, indicating an increase of the process zone size.

---

[1]We define the fracture energy G_R as the energy spent in the creation of unit (nominal) fracture surface.

[2]The fracture toughness K_{Ic} is calculated from Irwin's equation using the fracture energy $K_{Ic} = \sqrt{G_R E'}$, where E' is the plane-strain elastic modulus defined.
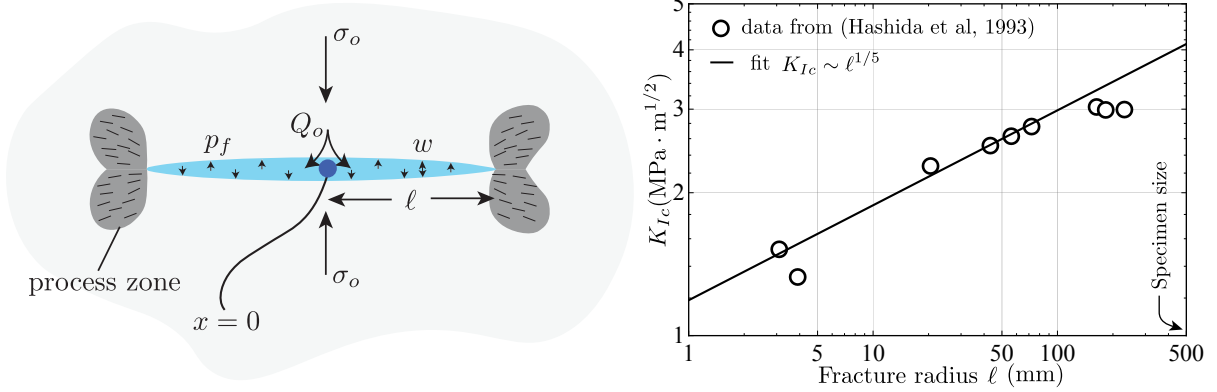
Fig. 1: Sketch of a hydraulic fracture with fracture length dependent apparent toughness (left) and the evolution of apparent toughness with fracture radius in hydraulic fracturing tests in Iidate granite from [18] (right). The evolution of the apparent toughness can be fitted by a power-law $K_{Ic} \propto \ell^{1/5}$ for $\ell < 100$ mm. The deviation for $\ell > 150$ mm might be possibly due to multiple reasons, such as the full development of the non-linear zone around the fracture tip and the restriction of the limited specimen size on the continuous growth of the apparent toughness.

Another line of observations comes from the analysis of magmatic dikes. Dikes are natural hydraulic fractures driven by magma, spanning a range of scale up to tens of kilometers. A recent review on dike propagation [20] reports that apparent fracture toughness values in the range 100-4000 MPa.m$^{1/2}$ are often needed to reconcile field observations [21, 22, 23, 24, 25]. These ranges of toughness are larger by 2-3 orders of magnitude than values O(1) MPa.m$^{1/2}$ measured in the laboratory rock fracture [26, 27]. Moreover, field observations indicate that the process zone of dikes can be much larger than those produced at the tips of tensile fractures at the laboratory scale and exhibit a direct proportionality with fracture dimension [20, 28, 29, 30]. Such observations imply further a scale-dependent or fracture length dependent characteristic of the apparent fracture energy. Scholtz [31] analyses the emplacement of dikes [32] and finds that a linear displacement-length scaling provides a better fit to the data rather than a square-root scaling [22, 21, 33, 32], from which he infers that the fracture toughness scales with the square-root of fracture length instead of being a constant rock property. The proposed linear scaling of mode I natural fractures happens to be consistent with the well known linear relation between fault length and accumulated slip (and damage zone) for shear type fractures (mode II/III) in the earth crust [34].

There is not yet a clear consensus among researchers regarding the evolution of fracture tough-

ness at large scales in quasi-brittle rocks in the upper earth crust [31, 35]. The complexity of various physical mechanisms contributes to multiple possible explanations [20, 35]: in-situ stress [12, 36, 37], rock tensile strength [12], rock mass scale [29], temperature [33, 37] and the enhanced viscous losses due to roughness [38] are all reported more or less responsible for higher apparent toughness in hydraulic fractures at a larger scale. The goal of this paper is to quantify the impact of an increase of fracture energy with fracture length on HF propagation without presuming the exact toughening mechanism. We restrict ourselves to the case of an impermeable material and the injection at a constant rate Q_o of a Newtonian fluid of viscosity μ.

2. A power-law-like fracture length dependent toughness with a possible saturation

2.1. R-curve behaviour and its size effect

Numerous toughness measurements of quasi-brittle materials in the lab present a power-law like evolution of the fracture growth resistance as the fracture advances. Such increase then approaches a critical value – an evolution referred to as the "R-curve" [39]. This critical fracture growth resistance is commonly considered as a material property, which is presumed measurable when the specimen is large compared to the intrinsic material length scale (e.g. process zone size, which may possibly be much larger than typical laboratory samples). A size effect of the R-curve, though rarely mentioned in literature, has been reported in some experiments with specimen dimensions much larger than the ones typically used in the laboratory. Dempsey et al. [40] report a series of toughness measurements on sea ice plates, spanning from the common laboratory cm-m scale up to 80 m × 80 m, with the same plate width of 1.8 m for all specimens. The authors report an increase of the apparent fracture toughness with specimen dimensions up to 3 m × 3 m × 1.8 m with a value nearly twice the one measured on smaller specimens (0.5 m × 0.5 m × 1.8 m). Morel *et al.* findings [41] on wood also report a size effect of the R-curve behaviour. They show that the critical fracture resistance scales with the width of the cracked-through plate specimen and follows a power-law-like evolution with specimen width. Different from the observations on sea ice [40], no plateau value is reported in the evolution of the critical fracture resistance with specimen width, with a maximum thickness of 60 mm for all the geometrically self-similar specimens in their experiments. These findings, combined with observations from lab HF tests [18]

and dikes [31], imply a possible power-law evolution of the apparent fracture toughness and an existence of a finite toughness value beyond a certain length scale.

2.2. A power-law dependence of apparent fracture toughness

In this paper, we investigate the case where the apparent fracture energy follows a power-law-like fracture length dependence. We assume that the underlying increase of the process zone that results in the macroscopic increase of the apparent fracture toughness remains small compared to the fracture length. This hypothesis of small scale yielding [42] allows to approximate the fracture growth within the principles of linear elastic fracture mechanics (i.e. a single fracture characterised by the apparent fracture toughness). In terms of material toughness, we write

$$K_{Ic} = A\ell^{\alpha}, \quad A = \frac{K_*}{\ell_*^{\alpha}} \tag{1}$$

where K_* is the apparent fracture toughness measured at a given fracture length scale of ℓ_* and α the power-law scaling exponent. Such a power-law dependence does not introduce any new length scale as the pair of ℓ_* and K_* is selected so as to characterise the fracture length dependence of the toughness. Noticeably, such fracture length dependence of the apparent toughness is different from the one observed in a R-curve. In the R-curve, the evolution of the fracture growth resistance does not depend on the initial fracture length ℓ_o but is a function of the fracture extension length $\Delta\ell = \ell - \ell_o$ (the difference of the fracture length ℓ with respect to its initial value ℓ_o).

Different toughening mechanisms are embedded into such a power-law dependence model. The scaling exponent α is most likely function of material properties and in-situ conditions. According to [13, 43], the increase of the apparent toughness during the growth of a planar and smooth HF in weak formations is related to the size of plastic zone and depends on the level of in-situ stress, the rock strength and elastic modulus as well as the pumping parameters. It is therefore very likely that the power-law scaling exponent is function of these parameters as there are practical implications that the apparent fracture toughness will be higher when the fracture front propagates in the vertical than the horizontal directions [16, 43, 44, 45]. Such argument is consistent with the findings of [37] who report a dependence of the rock toughness on confining stresses. Morel et al. [41] also argue that the scaling exponent is material-dependent and is closely related to

5

self-affine fracture surfaces and their anomalous roughening characteristic. The through-the-plate fracture in their experiments initiates at a small length scale such that the initial fracture length in the propagation direction is much smaller than the length (perimeter) $\ell_\parallel$ of the fracture front (given by the plate thickness). In this case, the magnitude of the roughness increases as a function of the fracture length ℓ (case a). This results in an increasing discrepancy between the real fracture surface area at the micro scale and the nominal fracture surface at the macro scale. As a result, the fracture energy increases with the fracture length and presents a relation similar to Eq. (1), where α is function of self-affine scaling exponents of fracture surfaces. When the fracture length becomes comparable to the specimen width $\ell_\parallel$ in [41], the magnitude of the roughness saturates at a value dependent on $\ell_\parallel$ (case b). The toughness scaling changes to $K_{Ic} \propto \ell_\parallel^{\alpha_c}$, where α_c, also material-dependent and function of the self-affine scaling exponents, characterises the fracture roughness growth within the length of the fracture front $\ell_\parallel$. These observations (a and b) suggest different power-law scaling exponents for different fracture geometries. For a plane-strain hydraulic fracture in an infinite medium, the fracture front is infinite ($\ell_\parallel = \infty$), which suggests the apparent toughness scaling with the fracture length $K_{Ic} \propto \ell^\alpha$ as in case (a). For a radial fracture, the fracture length (radius) is comparable to the front length ($\ell_\parallel = 2\pi\ell$), suggesting the apparent toughness scaling with fracture radius, $K_{Ic} \propto \ell_\parallel^{\alpha_c}$, as in case (b). We compile different power-law scaling exponents of different materials from the literature in Table 1. The exponents for granite and mortar are obtained based on the argument of [41] and roughness self-affine scaling exponents in [46, 47]. Moreover, a power-law scaling exponent of $\alpha \approx 1/2$ is suggested [32] based on the field observations of emplacement scaling on dikes and a value of $\alpha \approx 0.1$ for Nevada Tuff is also reported [35] from laboratory measurements [48].

2.3. Possible appearance of a finite apparent toughness beyond a length scale

The exact evolution of apparent fracture toughness with fracture length remains an open question. As reported in the previously mentioned experiments [18, 40], the toughening effect is likely curtailed beyond a certain length scale ℓ_s (fracture length beyond which the apparent toughness reaches an asymptotic value). Such an upper limit of the increase of apparent toughness may result from different mechanisms. Papanastasiou [13, 15] examines the apparent fracture toughness of a

Table 1: Power-law scaling exponents for the evolution of apparent fracture toughness for different materials and geometries. The power-law exponents for plane-strain and axisymmetric fractures are estimated by using Eq. (4.6) and Eq. (4.7) in [41] respectively and using the roughness self-affine scaling exponents in [41] for pine and spruce, [46] for granite and [47] for mortar.

Material	Plane-strain (α)	Axisymmetric (α_c)
Pine	0.062-0.183	0.365
Spruce	0.055-0.131	0.235
Granite	0.171	0.205
Mortar	0.039	0.275

smooth plane-strain HF in an infinite domain using a coupled elasto-plastic finite element model with cohesive interface elements for propagation criterion. The author shows that the apparent toughness increases initially with fracture length following approximately a power law, and then reaches an asymptotic value. The author owes the observed plateau of the apparent toughness to the full development of plastic(or process) zones that shield the tip. However, the appearance of the finite toughness is also possibly due to the restraints of the specimen(or crust) dimensions. If we account for the fracture roughness and extend the findings in [41] to large scale fractures, a potentially unabated fracture toughening with fracture growth is expected for an unbounded domain. However, when the fracture grows close to the specimen (or earth crust) dimensions in the lab (or at depth), a finite apparent toughness may also appear due to such dimension limit on the continuous growth of apparent toughness. It may be likely that the saturation length scale ℓ_s can be potentially large given that the large toughness values reported in dikes [21, 22, 23, 24, 25] correspond to a fracture length of the order of kilometers.

In the following, we investigate the growth of a fluid-driven fracture assuming a power-law dependence of toughness with fracture length as described by Eq. (1) and also account for a possible saturation of the fracture toughness above a given scale. We focus on both plane-strain and axisymmetric (radial) fracture geometries. We first perform a dimensional analysis to describe the solution structure as well as the governing dimensionless parameters. We then solve the complete evolution problem numerically. We notably develop a scheme combining a Gauss-Chebyshev

quadrature with Barycentric Lagrange interpolation and differentiation techniques [49]. In Section 3, 4, 6, 7.1 and 7.2, we assume that the saturation length scale ℓ_s is very large ($\ell_s \rightarrow \infty$) so that the toughness follows a power-law-like evolution without reaching the asymptotic value ($\ell < \ell_s$). We then discuss the effect of the plateau of apparent fracture toughness beyond a saturation length scale ℓ_s in Section 7.3.

3. Mathematical model

We introduce a parameter d in order to represent the governing equations for a plane-strain ($d = 1$) and an axisymmetric hydraulic fracture ($d = 2$) simultaneously. In view of the problem symmetry, we write the governing equations for the fracture half-length $\ell(t)$ in plane-strain, and also denote the fracture radius as $\ell(t)$ for the axisymmetric / radial geometry. Following [50, 51], we use the following set of effective material parameters for clarity:

$$K'_* = \sqrt{\frac{32}{\pi}} K_*, \quad E' = \frac{E}{1 - \nu^2}, \quad \mu' = 12\mu \tag{2}$$

where E is the solid elastic modulus, ν Poisson's ratio, μ the fluid viscosity, and K_* the reference apparent fracture toughness measured at $\ell = \ell_*$.

3.1. Elasticity

For a strictly Mode I fracture, the elasticity equations reduce to a single boundary integral equation relating the fracture opening w and the net pressure p defined as $p = p_f - \sigma_o$ where σ_o is the in-situ compressive stress normal to the fracture plane (the minimum stress) [52]:

$$\frac{1}{4\pi} \frac{1}{\ell} \int_{-1}^{1} G_d(\xi, \xi') \frac{\partial w}{\partial \xi'} d\xi' = \frac{1}{E'} p, \quad \xi \in [-1, 1] \tag{3}$$

where $\xi = x/\ell$ is the dimensionless spatial coordinate in the fracture. G_d is the elastic kernel, representing the stress component normal to the fracture plane induced by a unit dislocation. It is function of the fracture geometry:

- In plane-strain ($d = 1$)

$$G_1(\xi, \xi') = \frac{1}{\xi - \xi'} \tag{4}$$

8

- and in axisymmetry ($d = 2$)

$$G_2(\xi,\xi') = \begin{cases} \text{sign}(\xi\xi') \left[\dfrac{1}{\xi - \xi'} \mathbf{E}(k) - \dfrac{1}{\xi} \mathbf{K}(k) \right], & |\xi'| < |\xi| \\[2ex] \dfrac{1}{\xi - \xi'} \mathbf{E}(1/k), & |\xi'| > |\xi| \end{cases} \tag{5}$$

where $k = \xi'/\xi$ and $\mathbf{E}(k)$ and $\mathbf{K}(k)$ denote the complete elliptic integrals. The axisymmetric kernel is obtained from the solution for a ring dislocation at $\xi' \in [0,1]$ [53, 54], and the symmetric continuation onto $\xi' \in [-1,0]$.

3.2. Lubrication flow

The elastic compliance of an open fracture is much larger than the fluid compressibility [55]. As a result, under the assumption of an impermeable medium (zero leak-off) and zero fluid lag, the width-averaged fluid mass conservation reduces to volume conservation:

$$\frac{\partial w}{\partial t} + \frac{1}{x^{d-1}} \frac{\partial}{\partial x} \left(x^{d-1} q \right) = 0 \tag{6}$$

Similarly, for laminar flow conditions, the width averaged fluid balance of momentum reduces to Poiseuille law relating the local fluid flux q to the local pressure gradient [56]:

$$q = -\frac{w^3}{\mu'} \frac{\partial p}{\partial x} \tag{7}$$

where we have implicitly assumed that the in-situ compressive stress σ_o is uniform.

3.3. Boundary conditions

The fluid is injected at the fracture center $x = 0$ either as a line ($d = 1$) or a point ($d = 2$) source. We assume a constant injection rate Q_o in the following. A zero fluid flux and zero fracture opening conditions apply at the fracture tip $x = \ell$ [57]:

$$2 \lim_{x/\ell \to 0} (\pi x)^{d-1} q = Q_o, \quad q(\ell) = 0, \quad w(\ell) = 0 \tag{8}$$

3.4. Global continuity equation

The integration of the lubrication equation (6) combined with the previous boundary conditions (8) yield a global fluid continuity equation:

$$2 \int_0^\ell (\pi x)^{d-1} w \mathrm{d}x = Q_o t \tag{9}$$

9

3.5. Propagation criterion

Under the assumption of small scale yielding, the process zone size is much smaller than the fracture length and linear elastic fracture mechanics is valid to describe the fracture propagation. The propagation criterion of a quasi-static hydraulic fracture translates into the classical square-root asymptote near the fracture tip [42], with the mode I stress intensity factor K_I equal to the fracture toughness K_{Ic} at all time: $K_I = K_{Ic}$. In view of the fracture length dependent evolution of the toughness described by the power law in Eq. (1), the linear elastic fracture mechanics asymptote for fracture width near the tip becomes:

$$w \sim \frac{K'_*}{E'}\left(\frac{\ell}{\ell_*}\right)^{\alpha}(\ell - x)^{1/2}, \quad \ell - x \ll \ell \tag{10}$$

4. Scalings and Structure of the solution for a fracture-length-dependent toughness

4.1. Viscosity and toughness scaling

The propagation of plane-strain and radial hydraulic fractures are well understood for the case of fracture length independent fracture toughness. Solutions [58, 59, 50] have been obtained in limiting propagation regimes where either the dissipation associated with fluid viscous flow (viscosity dominated - $M-$regime) or with the creation of new fracture surfaces (toughness dominated - $K-$regime). For the case of a plane-strain hydraulic fracture in an impermeable medium, the propagation is actually always self-similar and is defined by a single dimensionless parameter characterising the relative importance of toughness versus viscous forces: e.g. a dimensionless toughness $\mathcal{K}$. The radial fracture geometry yields a different solution structure. Indeed, as the perimeter of the fracture increases with time, the energy associated with the creation of new surfaces increases and eventually dominates over viscous forces at large time. As a result, for a radial fracture, the dimensionless toughness $\mathcal{K}$ increases with time: the propagation transitions from the $M-$regime to the $K-$regime. In what follows, using similar procedures, we investigate the scaling of the solution for both geometries in the case of a fracture length dependent fracture toughness and discuss the corresponding modifications of the structure of the propagation of a hydraulic fracture in an impermeable medium.

We introduce a dimensionless fracture opening Ω, net pressure Π, and fracture half-length or fracture radius γ as follows:

$$\ell(t) = L(t)\gamma(\xi, \mathcal{G}), \quad w(x,t) = \epsilon(t)L(t)\Omega(\xi, \mathcal{G}), \quad p(x,t) - \sigma_o = \epsilon(t)E'\Pi(\xi, \mathcal{G}) \tag{11}$$

In these definitions, $\epsilon(t)$ is a small dimensionless number capturing the fact that the fracture characteristic scale $W(t)$ is much smaller than the characteristic length $L(t)$. Similarly the characteristic net pressure $P(t) = \epsilon(t)E'$ is much smaller than the rock elastic modulus. $\mathcal{G}(t)$ denotes additional dimensionless parameters of which the solution depends on. All yet to be defined and possibly dependent on time to reflect the moving boundary nature of the hydraulic fracture problem.

With such a scaling, we thus obtain the following dimensionless form of the governing equations.

- Elasticity

$$\frac{1}{4\pi}\frac{1}{\gamma}\int_{-1}^{1} G_d(\xi,\xi')\frac{\partial\Omega}{\partial\xi'}d\xi' = \Pi(\xi) \tag{12}$$

- Lubrication flow (Reynold's equation obtained combining fluid continuity and Poiseuille law) written in the moving coordinates system ($\xi = x/\ell(t)$):

$$\left(\frac{\dot{\epsilon}t}{\epsilon} + \frac{\dot{L}t}{L}\right)\Omega - \frac{\dot{L}t}{L}\xi\frac{\partial\Omega}{\partial\xi} + \dot{\mathcal{G}}t\left(\frac{\partial\Omega}{\partial\mathcal{G}} - \frac{\xi}{\gamma}\frac{d\gamma}{d\mathcal{G}}\frac{\partial\Omega}{\partial\xi}\right) = \frac{1}{\mathcal{G}_m}\frac{1}{\gamma^2\xi^{d-1}}\frac{\partial}{\partial\xi}\left(\xi^{d-1}\Omega^3\frac{\partial\Pi}{\partial\xi}\right) \tag{13}$$

- Global continuity equation

$$2\pi^{d-1}\gamma^d\int_0^1 \xi^{d-1}\Omega d\xi = \mathcal{G}_v \tag{14}$$

- Propagation condition (in terms of the fracture width near-tip asymptote) for the case of a power-law dependence of the fracture toughness on the fracture length (Eq. (1)):

$$\Omega \sim \mathcal{G}_k\gamma^{\alpha+1/2}(1 - \xi)^{1/2}, \quad 1 - \xi \ll 1 \tag{15}$$

In these dimensionless equations, $\mathcal{G}_m$, $\mathcal{G}_v$ and $\mathcal{G}_k$ are three independent dimensionless groups emerging from lubrication flow, global continuity and propagation criterion respectively, whose expressions are given by:

$$\mathcal{G}_m = \frac{\mu'}{\epsilon^3 E' t}, \quad \mathcal{G}_v = \frac{Q_o t}{\epsilon L^{d+1}}, \quad \mathcal{G}_k = \frac{K'_*}{\epsilon E' L^{1/2}}\left(\frac{L}{\ell_*}\right)^\alpha \tag{16}$$

11

Table 2: Viscosity and toughness scaling for plane-strain ($d = 1$) and radial ($d = 2$) hydraulic fractures in the case of a power-law dependence of fracture toughness with fracture length.

Scaling	Viscosity	Toughness
$\epsilon(t)$	$\epsilon_m = \left(\dfrac{\mu'}{E't}\right)^{1/3}$	$\epsilon_k = \left(\dfrac{K'^{d+1}_*}{E'^{d+1}Q_o^{1/2-\alpha}\ell_*^{\alpha(d+1)}t^{1/2-\alpha}}\right)^{1/(\alpha+d+1/2)}$
$L(t)$	$L_m = \left(\dfrac{E'Q_o^3t^4}{\mu'}\right)^{1/(3(d+1))}$	$L_k = \left(\dfrac{Q_oE'\ell_*^{\alpha}t}{K'_*}\right)^{1/(\alpha+d+1/2)}$
$W(t)$	$W_m = \left(\dfrac{\mu'^dQ_o^3t^{3-d}}{E'^d}\right)^{1/(3(d+1))}$	$W_k = \left(\dfrac{K'^d_*Q_o^{\alpha+1/2}t^{\alpha+1/2}}{E'^d\ell_*^{\alpha d}}\right)^{1/(\alpha+d+1/2)}$
$P(t)$	$P_m = \left(\dfrac{E'^2\mu'}{t}\right)^{1/3}$	$P_k = \left(\dfrac{K'^{d+1}_*}{E'^{1/2-\alpha}Q_o^{1/2-\alpha}\ell_*^{\alpha(d+1)}t^{1/2-\alpha}}\right)^{1/(\alpha+d+1/2)}$
$\mathcal{G}(t)$	$\mathcal{G}_m = 1$ $\mathcal{G}_k = \mathcal{K} = (t/t_{mk})^{(d-1+4\alpha)/(3(d+1))}$	$\mathcal{G}_m = \mathcal{M} = (t/t_{mk})^{-(d-1+4\alpha)/(\alpha+d+1/2)}$ $\mathcal{G}_k = 1$

₂₃₀ In order to define a particular scaling, we set two of these dimensionless groups to unity and
₂₃₁ solve for the corresponding $\epsilon(t)$ and $L(t)$. For an impermeable medium, the fracture volume always
₂₃₂ equals the injected volume, i.e. $\mathcal{G}_v = 1$. Two scalings are therefore obtained by assuming that
₂₃₃ either viscous forces ($\mathcal{G}_m = 1$) or toughness ($\mathcal{G}_k = 1$) dominate. It results in a viscosity and a
₂₃₄ toughness scaling respectively. Table 2 lists the different characteristic scales and dimensionless
₂₃₅ parameters in these two scalings as functions of the material parameters, injection rate, time and
₂₃₆ fracture geometry.

₂₃₇ In the viscosity scaling, $\mathcal{G} = \mathcal{G}_k$ is the only remaining dimensionless parameter appearing in
₂₃₈ the set of governing equations which we rename as dimensionless toughness $\mathcal{K}$. It characterises
₂₃₉ the relative importance of the solid apparent toughness compared to viscosity on the propagation
₂₄₀ of a hydraulic fracture. In the toughness scaling, we define similarly the dimensionless viscosity
₂₄₁ $\mathcal{M}$ from $\mathcal{G} = \mathcal{G}_m$. The scalings are of course related to one another - via the following relations:

$$\mathcal{K} = \left(\frac{t}{t_{mk}}\right)^{(d-1+4\alpha)/(3(1+d))}, \quad \mathcal{M} = \mathcal{K}^{-3(1+d)/(\alpha+d+1/2)}, \quad \frac{\epsilon_m}{\epsilon_k} = \mathcal{K}^{-(d+1)/(\alpha+d+1/2)}, \quad \frac{L_m}{L_k} = \mathcal{K}^{1/(\alpha+d+1/2)}$$

(17)

₂₄₂ In the previous relation, we have introduced a timescale t_{mk}, which corresponds to the time when
₂₄₃ the characteristic fracture scales in the two scalings are equal, i.e. $L_m = L_k$ at $t = t_{mk}$. Such a

12

244 timescale quantifies the time of transition from the $M-$regime to the $K-$regime. We can define the

245 corresponding transitional characteristic scales $L_{mk} = L(t_{mk})$, $W_{mk} = W(t_{mk})$, and $P_{mk} = P(t_{mk})$:

$$t_{mk} = \left(\frac{\mu'^{d+\alpha+1/2}Q_o^{3/2-3\alpha}E'^{2d-\alpha+5/2}\ell_*^{3\alpha(d+1)}}{K_*'^{3(1+d)}}\right)^{1/(4\alpha+d-1)} \quad , \quad L_{mk} = \left(\frac{\mu'Q_oE'^3\ell_*^{4\alpha}}{K_*'^4}\right)^{1/(4\alpha+d-1)} \quad ,$$

$$W_{mk} = \left(\frac{\mu'^{\alpha+1/2}Q_o^{\alpha+1/2}E'^{5/2-d-\alpha}\ell_*^{\alpha(3-d)}}{K_*'^{(3-d)}}\right)^{1/(4\alpha+d-1)} \quad , \quad P_{mk} = \left(\frac{K_*'^{d+1}}{\mu'^{1/2-\alpha}Q_o^{1/2-\alpha}E'^{3/2-3\alpha}\ell_*^{\alpha(d+1)}}\right)^{1/(4\alpha+d-1)}$$

(18)

246   It is worthwhile to note that the viscosity scaling does not depend on fracture toughness. The

247 expressions obtained are similar to the ones derived in [58, 50]. Only the toughness dominated

248 scaling is modified compared to the case of the fracture length independent toughness. By setting

249 $\alpha = 0$, we obviously recover the well-known scalings for the case of the fracture length indepen-

250 dent fracture toughness [58, 59, 50]. For example, in a plane-strain fracture ($d = 1$), when the

251 fracture toughness is fracture length independent $\alpha = 0$, the dimensionless toughness $\mathcal{K}$ becomes

252 time-independent

$$d = 1 : \mathcal{K}(\alpha = 0) = \frac{K_*'}{E'}\left(\frac{E'}{\mu'Q_o}\right)^{1/4}$$

(19)

253 coincident with the expression obtained in [58, 59].

4.2. Zero-viscosity / toughness dominated solutions

255   The fracture propagation problem reduces to a self-similar problem at small ($\mathcal{K} \ll 1$) and large

256 time ($\mathcal{K} \gg 1$). The early-time viscosity dominated solutions already available in the literature are

257 of course also valid for the case of fracture length dependent toughness (fracture toughness does

258 not play a role in the viscosity dominated regime). We derive here large-toughness solutions in a

259 similar manner as in the case of fracture length independent toughness [60, 50, 58]. These zero

260 viscosity solutions are expressed in the toughness scalings, and the corresponding dimensionless

261 opening, length and net pressure are referred with a subscript *ko* in reference to the zero-viscosity

262 solutions. As the viscosity is negligible, the net pressure is uniform in the fracture. The governing

263 equations reduce to the elastic solution for a uniformly pressurized fracture, global volume balance

13

and fracture propagation condition, i.e.:

$$\Omega_{ko} = 4\left(\frac{2}{\pi}\right)^{d-1} \gamma_{ko}\Pi_{ko} \sqrt{1-\xi^2} \tag{20}$$

$$2\gamma_{ko}^d \int_0^1 (\pi\xi)^{d-1}\Omega_{ko}\mathrm{d}\xi = 1 \tag{21}$$

$$\Omega_{ko} \sim \gamma_{ko}^{\alpha+1/2}(1-\xi)^{1/2}, \quad 1-\xi \ll 1 \tag{22}$$

where Ω_{ko}, γ_{ko} and Π_{ko} are the dimensionless fracture opening, fracture half-length ($d = 1$) or fracture radius ($d = 2$), and net pressure. The solutions for a plane-strain fracture are thus

$$\gamma_{ko} = \left(\frac{2\sqrt{2}}{\pi}\right)^{1/(\alpha+3/2)} , \; \Pi_{ko} = \frac{1}{2\pi}\left(\frac{\pi}{2\sqrt{2}}\right)^{2/(\alpha+3/2)} , \; \Omega_{ko} = \frac{2}{\pi}\left(\frac{\pi}{2\sqrt{2}}\right)^{1/(\alpha+3/2)} \sqrt{1-\xi^2} \tag{23}$$

and for an axisymmetric fracture:

$$\gamma_{ko} = \left(\frac{3}{\pi\sqrt{2}}\right)^{1/(\alpha+5/2)} , \; \Pi_{ko} = \frac{3}{16}\left(\frac{\pi\sqrt{2}}{3}\right)^{3/(\alpha+5/2)} , \; \Omega_{ko} = \frac{3}{2\pi}\left(\frac{\pi\sqrt{2}}{3}\right)^{2/(\alpha+5/2)} \sqrt{1-\xi^2} \tag{24}$$

We recover the zero-viscosity solutions for fracture length independent fracture toughness [59, 50] when setting $\alpha = 0$ in (23) and (24).

4.3. Effect of fracture length dependent toughness

One important difference brought by the fracture length dependent toughness ($\alpha > 0$) is that the dimensionless toughness increases with time in both geometries. This notably changes the partition between the viscous and the fracture energy dissipation during the growth of a hydraulic fracture even for a plane-strain fracture. In both geometries, as the fracture toughness increases with length, the energy spent in the creation of new fracture surface necessarily increases with time and ultimately dominates. This constitutes a qualitative change in the evolution of plane-strain HF from the case with fracture length independent toughness, when the dissipation partition is time-invariant. A plane-strain hydraulic fracture will eventually transition to the toughness dominated regime for the case of unabated increase of the apparent fracture toughness, even if it is initially dominated by viscosity.

For a radial fracture, the transition from the viscosity to the toughness dominated regime is accelerated due to the increase of the fracture toughness with fracture length. Larger α implies a

14

faster increase of the energy dissipated in the solid and leads to a smaller value of the transition timescale t_{mk}. The increase of the fracture energy results in a higher net pressure required to drive the fracture propagation. Smaller fracture length and wider fracture opening are obtained for the same volume of the injected fluid.

It is interesting to note that when $\alpha = 1/2$, $\mathcal{K} \propto (t/t_{mk})^{1/3}$, for both geometries (Table 2). Notably for that particular value of α, the characteristic pressure scale $P_k(t)$ becomes independent of time, i.e. the propagation is driven by a constant pressure at large time: this pressure exactly balance the toughness increase with length. For values of the power-law scaling exponent α larger than $1/2$, we observe that the characteristic toughness dominated pressure $P_k(t)$ increases with time for both geometries. This is a significant difference compared to the fracture length independent toughness case. In other words, for $\alpha > 1/2$, the increase of the stress intensity with fracture length (in $\propto P_k \ell^{1/2}$) is not sufficient to compensate the increase of the toughness with length (in $\propto \ell^\alpha$ from Eq. (1)). Classically in hydraulic fracturing, a net pressure increase with time is related to the propagation of a height contained / blade-like fracture (also referred to as the PKN geometry) under the assumption of a fracture length independent toughness [61]. Existing field observations of net pressure increases are usually relatable to contained-height hydraulic fracture growth (PKN fracture) as monitored by micro-seismicity [62]. It is thus interesting to contrast such a behaviour for very different fracture geometry (radial or plane-strain) for a power-law dependent toughness with $\alpha > 1/2$. We therefore see that in the field in order to decipher between these two possible causes, independent measurements of fracture geometry and pressure are required.

5. Numerical algorithm

We now describe a numerical method for the solution of the complete evolution problem from a given initial state - e.g. the viscosity dominated solution which is valid for time smaller than $t_{mk}(\alpha)$. Our method is based on a non-uniform moving mesh discretized using a Gauss-Chebyshev quadrature and a collocation method [63, 49].

Extrapolation, integration, and differentiation operations are simplified as matrix multiplications using Barycentric techniques [64, 49]. We turn the fully coupled hydraulic fracture propagation problem into a system of ordinary differential equations in time that can be integrated with

15

classical methods for ordinary differential equations.

We first present the Gauss-Chebyshev quadratures associated with the discretization of the elastic equation. We then select the corresponding Barycentric operators listed in [49] and show how they can be applied to the discretization of a radial and plane-strain fracture. The corresponding vector and matrix are denoted respectively by bold type and blackboard bold type.

5.1. Gauss-Chebyshev quadrature

Gauss-Chebyshev quadrature methods for the solution of boundary integral equation arising in fracture mechanics is a classical technique [63]. The method makes use of a primary $\mathbf{s} = \{s_j\}, j = 1,...,n$, and a complimentary $\mathbf{z} = \{z_i\}, i = 1,...,m$, sets of nodes, discretizing the fracture interval $(-1,1)$, which corresponds to the roots of the respective Chebyshev polynomials denoted as $\phi_n(s)$ and $\psi_m(z)$ respectively [63]. The choice of $\phi_n(s), \psi_m(z)$ and corresponding sets of nodes $\mathbf{s}$ and $\mathbf{z}$ stems from the type of the dislocation density singularity at the fracture tips. Specifically, the square-root singularity of linear elastic fracture mechanics can be directly embedded in the discretization. The dislocation density is expressed as:

$$\frac{\mathrm{d}w}{\mathrm{d}s} = \omega(s)F(s), \quad \omega(s) = \frac{1}{\sqrt{1 - s^2}} \tag{25}$$

where $\omega(s)$ is a weight function with the required tip singularity and $F(s)$ an unknown non-singular function.

For the type of singularity embedded in Eq. (25), the primary and complimentary polynomials are the Chebyshev's of the first $\phi_n(s) = T_n(s)$, and second $\psi_m(z) = U_m(z)$ (with $m = n - 1$) kinds respectively; and the two sets of spatial nodes are given by:

$$s_j = \cos\left(\frac{\pi(j - 1/2)}{n}\right), j = 1,...,n; \quad x_i = \cos\left(\frac{\pi i}{n}\right), i = 1,...,n - 1, \tag{26}$$

5.2. Hilbert transform operator for the dislocation density

The Hilbert transform

$$\mathcal{H}[w](z) = \frac{1}{\pi} \int_{-1}^{1} \frac{1}{z - s} \frac{\partial w}{\partial s} \mathrm{d}s \tag{27}$$

16

is evaluated on the complimentary $\mathbf{z}$−set of nodes using representation (25) of the dislocation density on the $\mathbf{s}$−set, $\{F(s_j)\}$. This results in the following:

$$\mathcal{H}[w](z_i) = \sum_{j=1}^{n} H_{ij}F(s_j), \quad H_{ij} = \frac{1}{n}\frac{1}{z_i - s_j} \tag{28}$$

5.3. Operators for extrapolation, differentiation and integration

The unknown function F representing the unknown dislocation density as Eq. (25) can be extrapolated from the Gauss-Chebyshev nodes to the fracture tip:

$$F(-1) = \sum_{j=1}^{n} P_jF(s_j), \quad F(1) = \sum_{j=1}^{n} Q_jF(s_j) \tag{29}$$

where, according to Table 3 of [49].

$$P_j = (-1)^j \frac{\tan(\arccos(s_j)/2)}{n}, \quad Q_j = -(-1)^j \frac{\cot(\arccos(s_j)/2)}{n} \tag{30}$$

Integration operators can be defined on either grid with the result of integration on the same or the other grid. For example, consider the integration of a regular function $g(s)$ defined on the $\mathbf{z}$−grid, $\{g(z_i)\}$, with the result evaluated on the same grid:

$$\int_0^{z_i} g(z)\mathrm{d}z = \sum_{i'=1}^{m} T_{ii'}g(z_{i'}), \quad T_{ii'} = \sum_{k=0}^{m-1}[\Psi_k(z_i) - \Psi_k(0)]B_{ki'} \tag{31}$$

where, from Table 2 in [49], $\Psi_k(z)$ is the indefinite integral of the complimentary set of Chebyshev's polynomials (i.e. $\psi_k = U_k(z)$),

$$\Psi_k(z) = \int^z \psi_k(z)\mathrm{d}z = \frac{\cos(k+1)\theta}{k+1}, \quad \theta = \arccos(z) \tag{32}$$

and

$$B_{ki'} = \frac{2}{m+1}\sin\left(\frac{\pi i'}{m+1}\right)\sin\left(\frac{\pi(k+1)i'}{m+1}\right) \tag{33}$$

For another example, consider integration of the dislocation density $\mathrm{d}w/\mathrm{d}s = \omega(s)F(s)$, with $F(s)$ defined on the $\mathbf{s}$−grid, $\{F(s_j)\}$, and results evaluated on the $\mathbf{z}$−grid [49]:

$$\int_{z_i}^{+1} \frac{\partial w}{\partial s}\mathrm{d}s = -\sum_{j=1}^{n} S_{ij}F(s_j), \quad S_{ij} = \sum_{k=0}^{n-1}[\Phi_k(z_i) - \Phi_k(1)]B_{kj} \tag{34}$$

17

where, from Table 2 in [49],

$$\Phi_k(z) = \int^z \phi_k(s)\mathrm{d}s = -\frac{\sin k\theta}{k} \tag{35}$$

and

$$B_{kj} = \begin{cases} \dfrac{1}{n}, & k = 0 \\ \dfrac{2}{n}\cos\left(\dfrac{\pi k(j - 1/2)}{n}\right), & k > 0 \end{cases} \tag{36}$$

Specifically, the integration matrix $\{S_{ij}\}$ simplifies to a vector $\{S_{Aj}\}$ on the integration interval $[-1,1]$ and simplifies to $\{S_{Hj}\}$ on $[0,1]$.

$$\int_{-1}^{+1} \frac{\partial w}{\partial s}\mathrm{d}s = \sum_{j=1}^{n} S_{Aj}F(s_j), \quad S_{Aj} = \sum_{k=0}^{n-1}[\Phi_k(1) - \Phi_k(-1)]B_{kj} \tag{37}$$

$$\int_{0}^{+1} \frac{\partial w}{\partial s}\mathrm{d}s = \sum_{j=1}^{n} S_{Hj}F(s_j), \quad S_{Hj} = \sum_{k=0}^{n-1}[\Phi_k(1) - \Phi_k(0)]B_{kj} \tag{38}$$

A differentiation operator can be defined on either grid. In the following, we utilize differentiation on the $\mathbf{z}$−grid. For a regular function $g(z)$, we obtain

$$g'(z_i) \approx \sum_{i'=1}^{m} D_{ii'}g(z_i); \quad D_{ii'} = \frac{\omega_{i'}/\omega_i}{z_i - z_{i'}}, \quad i \neq i'; \quad D_{ii} = -\sum_{i'=1,i'\neq i}^{m} D_{ii'} \tag{39}$$

where $\omega_i = (-1)^i\sin^2(\pi i/n)$ (see Table 3 in [49]).

5.4. Discretized governing equations

Using the previously defined operators, we discretize the governing equations of the problem as follows.

5.4.1. Elasticity

The elasticity equation (3) after discretization reads:

$$\frac{4\ell}{E'}p(z_i) = \sum_{j=1}^{n} \frac{1}{n}G_d(z_i,s_j)F(s_j) \tag{40}$$

written in the matrix form as:

$$\frac{4\ell}{E'}\mathbf{p} = \mathbb{G}_d \cdot \mathbf{F} \tag{41}$$

18

where $\mathbf{p} = \{p(z_i)\}$, $\mathbf{F} = \{F(s_j)\}$ are unknown vectors and $\mathbb{G}_d = \{\frac{1}{n}G_d(z_i, s_j)\}$ is the elasticity quadrature matrix.

The quadrature (40) has spectral accuracy for the plane-strain fracture [49, 63], when kernel $G_1(z,s) = \dfrac{1}{z-s}$ is the Cauchy one, and the corresponding quadrature matrix $\mathbb{G}_1 = \mathbb{H} = \{\dfrac{1}{n}\dfrac{1}{z_i - s_j}\}$.

For an axisymmetric fracture, the kernel is to the leading order of the Cauchy type, but it also contains a weaker logarithm singularity. We therefore write it as:

$$G_2(z,s) = \frac{1}{z-s} + \frac{\ln|z-s|}{2z} + \Delta G(z,s) \tag{42}$$

where $\Delta G(z,s)$ corresponds to the non-singular part of $G_2(z,s)$. In order to maintain the accuracy of the quadrature in this case, we represent the logarithm-term as an integral of the Cauchy-like term, $\ln|z-s| = \int_0^z \dfrac{\mathrm{d}z}{z-s} + \ln s$, where the latter term is inconsequential (i.e. it gives zero contribution to the elasticity integral). Using integration on the $\mathbf{z}$−grid for the logarithm-term, the final elasticity matrix for the axisymmetric fracture case becomes:

$$\mathbb{G}_2 = \mathbb{H} + \frac{1}{2\mathbf{z}}\mathbb{T} \cdot \mathbb{H} + \Delta\mathbb{G} \tag{43}$$

where $\mathbb{T} = \{T_{ii'}\}$ is the $\mathbf{z}$−grid integration matrix and $\Delta\mathbb{G} = \{\frac{1}{n}\Delta G(z_i, s_j)\}$.

5.4.2. Lubrication flow

We integrate the lubrication equation (6) from the $\mathbf{z}$−grid nodes to the fracture tip accounting for the tip boundary condition $w(\xi = 1) = 0$ (Eq. (8)):

$$-\left(\frac{\partial w_i}{\partial t}\frac{1}{d}z_i^d + \frac{\partial}{\partial t}\frac{1}{d}\int_{z_i}^1 \xi^d \frac{\partial w}{\partial \xi}\mathrm{d}\xi\right) - \frac{\dot{\ell}}{\ell}\int_{z_i}^1 \xi^d \frac{\partial w}{\partial \xi}\mathrm{d}\xi = -\frac{1}{\mu'\ell^2}z_i^{d-1}w_i^3\left.\frac{\partial p}{\partial \xi}\right|_{\xi=z_i} \tag{44}$$

where w_i is the fracture opening evaluated at z_i. The discretization of these terms is obtained in the following by using the integration operator $\mathbb{S} = \{S_{ij}\}$ and differentiation operator $\mathbb{D} = \{D_{ii'}\}$ and by back-substituting the discretized elasticity equation (40).

$$\left\{\frac{\partial w_i}{\partial t}\frac{1}{d}z_i^d\right\} = \frac{1}{d}\mathbf{z}^d \frac{\partial}{\partial t}(\mathbb{S} \cdot \mathbf{F}) \tag{45}$$

$$\left\{\frac{1}{d}\int_{z_i}^1 \xi^d \frac{\partial w}{\partial \xi}\mathrm{d}\xi\right\} = \frac{1}{d}\left(-\mathbb{S} \cdot \left(\mathbf{s}^d \mathbf{F}\right)\right) \tag{46}$$

$$\left\{\frac{1}{\mu'\ell^2}w_i^3 z_i^{d-1}\left.\frac{\partial p}{\partial \xi}\right|_{\xi=z_i}\right\} = \frac{E'}{4\mu'\ell^3}(\mathbb{S} \cdot \mathbf{F})^3 \mathbf{z}^{d-1}(\mathbb{D} \cdot \mathbb{G}_d \cdot \mathbf{F}) \tag{47}$$

19

We then obtain the final discretized $(n-1)$ lubrication equations:

$$-\frac{1}{d}\mathbf{z}^d \frac{\partial}{\partial t}(\mathbb{S} \cdot \mathbf{F}) + \frac{1}{d}\frac{\partial}{\partial t}\left(\mathbb{S} \cdot \left(\mathbf{s}^d\, \mathbf{F}\right)\right) + \frac{\dot{\ell}}{\ell}\left(\mathbb{S} \cdot \left(\mathbf{s}^d\, \mathbf{F}\right)\right) = -\frac{E'}{4\mu'\ell^3}(\mathbb{S} \cdot \mathbf{F})^3 \mathbf{z}^{d-1}\,(\mathbb{D} \cdot \mathbb{G}_d \cdot \mathbf{F}) \qquad (48)$$

5.5. Global continuity equation

The global continuity equation reduces to the following using the integration operators $\mathbf{S}_A = \{S_{Aj}\}$ or $\mathbf{S}_H = \{S_{Hj}\}$ defined above:

- Plane-strain

$$\int_{-1}^{1} \xi \frac{\partial w}{\partial \xi} d\xi + \frac{Q_o t}{\ell} = \mathbf{S}_A \cdot (\mathbf{s}\,\mathbf{F}) + \frac{Q_o t}{\ell} = 0 \qquad (49)$$

- Axisymmetry

$$\int_{0}^{1} \xi^2 \frac{\partial w}{\partial \xi} d\xi + \frac{Q_o t}{\pi \ell^2} = \mathbf{S}_H \cdot \left(\mathbf{s}^2\, \mathbf{F}\right) + \frac{Q_o t}{\pi \ell^2} = 0 \qquad (50)$$

5.6. Propagation criterion

The opening asymptote near the tip (10) indicates a square root singularity of the dislocation density at the tip as shown in Eq. (51), which is already embedded in the Gauss-Chebyshev quadrature (25):

$$\lim_{z \to 1} \frac{dw}{dz} = \lim_{z \to 1} \frac{dw}{d\xi}\frac{d\xi}{dz} = -\frac{K'_*}{E'}\frac{\ell^{1/2}}{2}\left(\frac{\ell}{\ell_*}\right)^{\alpha} \lim_{z \to 1} \frac{1}{\sqrt{1-z}} \qquad (51)$$

$$\lim_{z \to 1} \frac{dw}{dz} = \lim_{s \to 1}\omega(s)F(s) = \frac{F(1)}{\sqrt{2}}\lim_{s \to 1}\frac{1}{\sqrt{1-s}} \qquad (52)$$

By setting the coefficients before the singularity in Eq. (51) and Eq. (52) equal to each other and applying the extrapolation operator $\mathbf{Q} = \{Q_j\}$, the propagation condition for a fracture length dependent toughness simplifies to

$$F(1) \approx \mathbf{Q} \cdot \mathbf{F} = -\frac{1}{\sqrt{2}}\frac{K'_*\ell^{1/2}}{E'}\left(\frac{\ell}{\ell_*}\right)^{\alpha} \qquad (53)$$

We therefore get a set of discretized equations (48), (49) or (50) depending on the geometry, and (53), all of which are function of ℓ and $\mathbf{F}$. By differentiating Eq. (49) or (50), and Eq. (53) with respect to t, we finally get a system of ODEs that can be schematically written as:

$$\mathbb{M}(\mathbf{Y},t)\frac{d\mathbf{Y}}{dt} = \mathcal{F}(\mathbf{Y},t) \qquad (54)$$

where $\mathbf{Y} = \{\ell, \mathbf{F}\}$ is the unknown vector and $\mathbb{M}$ and $\mathcal{F}$ are the matrix and vector functions of $\mathbf{Y}$ and t which follow from the above differentiation.

On the account of the problem symmetry for a plane-strain fracture, choosing an even n, we set

$$\mathbf{F} = \{F_1, F_2, ..., F_{n/2}, -F_{n/2}, ..., -F_2, -F_1\} \tag{55}$$

The first $(n/2 - 1)$ equations of Eq. (48) are thus equivalent to the last $(n/2 - 1)$ equations. By taking advantage of the symmetry, we account for the first $(n/2 - 1)$ equations in Eq. (48) when building the ODEs of Eq. (54).

For a radial fracture, we select an odd n since the choice of an even n would result in infinite values of the elasticity matrix (43). We therefore set:

$$\mathbf{F} = \{F_1, F_2, ..., F_{(n-1)/2}, 0, -F_{(n-1)/2}, ..., -F_2, -F_1\} \tag{56}$$

Similarly, we take the first $((n - 1)/2 - 1)$ equations of Eq. (48) to build the ODE system.

The final non-linear system of ODEs (54) can be solved using appropriate numerical algorithms. We have used the built-in ODE solver of Mathematica 11.0 [65]. In terms of initial conditions, assuming a fracture length dependent toughness of Eq. (1), the fracture propagation for both geometries starts from a viscosity dominated solution[3]. We therefore use the solutions of the self-similar problem with $\mathcal{K} \ll 1$ for a plane-strain fracture (see Appendix A for more details) and the zero-toughness solution for a radial fracture [50]. In the latter, we initialize the fracture growth at time $t_o \ll t_{mk}(\alpha)$ with a fracture radius of $\ell_o \ll L_{mk}(\alpha)$ and a fracture toughness of $K_*(\ell_o/\ell_*)^\alpha$.

We use $n = 100$ for a plane-strain fracture and $n = 101$ for a radial fracture for all the simulations presented in this paper. The computational cost using the default settings of the Mathematica ODE solver is of several seconds for a simulation spanning 6-15 decades of time (e.g. two sec-

---

[3]If we account for a non-zero toughness at initiation, the approximation of zero-toughness solutions for a radial fracture is still valid at early time, since the energy dissipation in the solid is limited by the small geometry and viscosity dominates the fracture growth. However, this may differ for a plane-strain fracture: any state between the viscosity or toughness dominated regimes can serve as an initial condition, see Section 7.2 for more discussions.
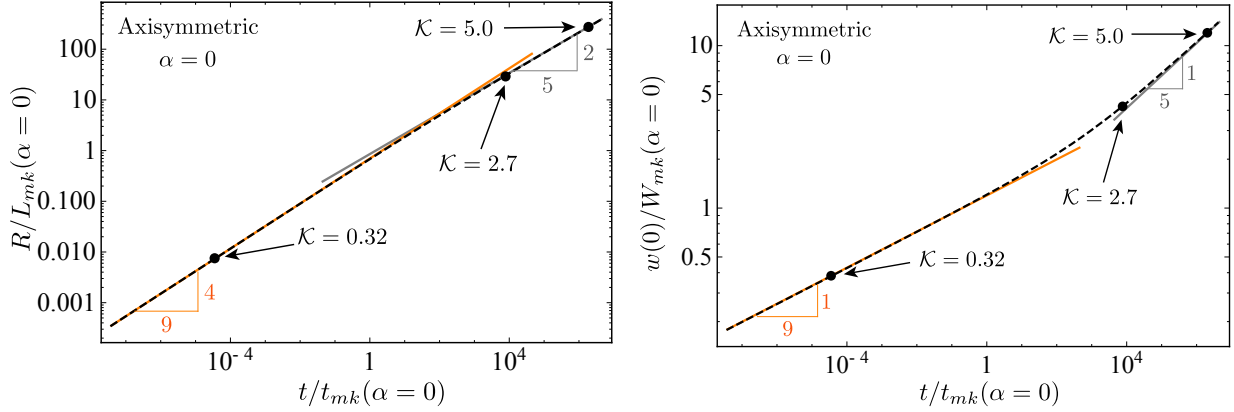
Fig. 2: Evolution of the dimensionless fracture radius and inlet opening with dimensionless time for the case of a fracture length independent toughness ($\alpha = 0$). Dashed curves indicate numerical solutions while the orange and gray lines correspond to zero-toughness ($\mathcal{K} = 0$) and zero-viscosity ($\mathcal{M} = 0$) solutions respectively.

onds for the case of Fig. 2, around 30 seconds for the case of Fig. 12)[4] on a personal computer (MacBook Pro, 2015, 2.9 GHz Intel Core i5).

5.7. Numerical verification - fracture length independent fracture toughness case

We first benchmark our numerical solver for the case of a fracture length independent fracture toughness for which a number of (semi-) analytical solutions are known. The solver is able to reproduce all propagation regimes for both geometries in a very efficient manner.

We present here comparisons for a radial fracture for which the solution evolves from viscosity to toughness dominated regime with time for a fracture length independent toughness.

The fracture behaviour is characterised by different power laws in the $M-$ and $K-$regime, as illustrated in Fig. 2, where the departure from the viscosity dominated regime is observed to start at t_{mk}. The profiles of the fracture opening and net pressure for $\mathcal{K} = 0.32, 2.7, 5.0$ are displayed in Fig. 3, showing an excellent match with the zero-toughness ($\mathcal{K} = 0$) and large-toughness ($\mathcal{M} \ll 1$) solutions [50] respectively.

---

[4]The computational cost is related to the complexity and non-linearity of the system. The system of Fig. 12 is more non-linear due to a smoothed toughness saturation function and is thus more time-consuming than the case of Fig. 2.
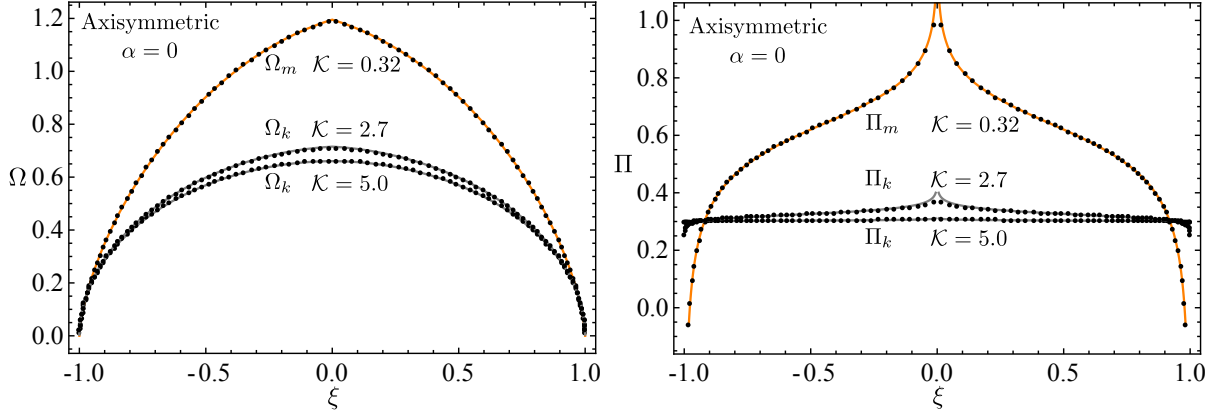
22

Fig. 3: Profile of fracture opening and net pressure in a radial fracture for the case of a fracture length independent toughness ($\alpha = 0$) with $\mathcal{K} = (t/t_{mk}(\alpha = 0))^{1/9} = 0.32, 2.7, 5.0$, scaled separately by viscosity scaling Ω_m, Π_m and toughness scaling Ω_k, Π_k. The near M−vertex solution ($\mathcal{K} = 0.32 \leq 1$ [50]) can be approximated the by zero-toughness solution which is indicated by the orange curve. The gray curves indicate the corresponding large-toughness solutions [50] with $\mathcal{K} = 2.7, 5.0$ respectively.

6. Results for fracture length dependent toughness

We now discuss the effect of a fracture length dependent toughness on the growth of hydraulic fractures for $\alpha \in [0, 1]$.

We first discuss the plane-strain geometry. Fig. 4 displays the evolution of fracture half-length, net pressure and width at the fracture inlet for different values of α. As observed from the scaling considerations discussed in Section 4, the hydraulic fracture propagation evolves from the viscosity to the toughness dominated regime. We observe from the simulation that the transition starts at time larger than $t_{mk}(\alpha)$ in line with the scaling arguments. At large time, the numerical solutions approximately coincide with the large toughness / zero viscosity asymptotes (blue lines on Fig. 4). A power-law dependence toughness leads to a shorter fracture length and larger net pressure in the toughness dominated regime. We observe a propagation under constant net pressure for $\alpha = 1/2$ and even an increase of net pressure with time for $\alpha > 1/2$ as expected.

Similar evolutions are observed for a radial hydraulic fracture. The time evolution of the fracture radius and inlet width are displayed in Fig. 5 for different α.

It is interesting to re-scale these numerical results using the viscosity scaling and to redefine the dimensionless toughness by using the current value of toughness $K_*(\ell/\ell_*)^\alpha$ as function of the
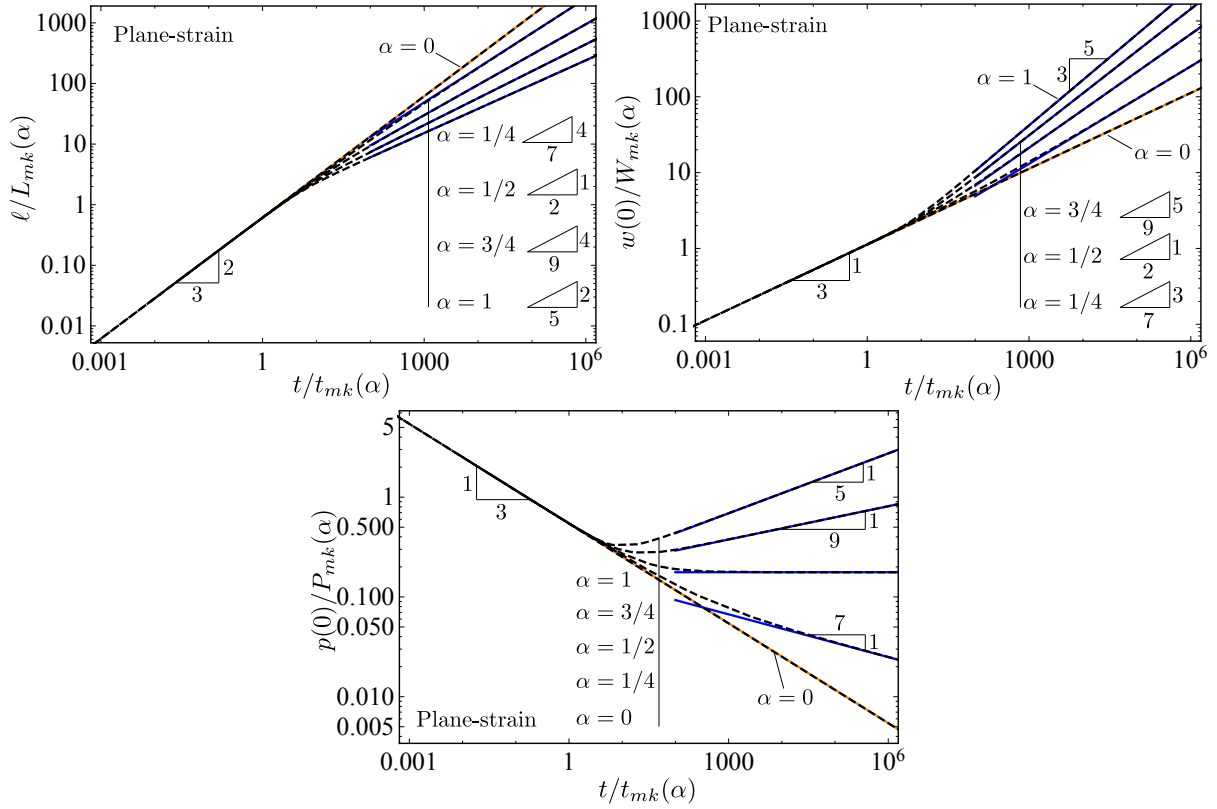
23

Fig. 4: Evolution of the dimensionless fracture half-length (up-left), inlet opening (up-right) and net pressure at the inlet (down) with dimensionless time in a plane-strain fracture, dashed curves indicate the numerical simulations while the blue solid lines indicate the fracture length dependent zero-viscosity solutions and orange solid lines the viscosity dominated solutions.
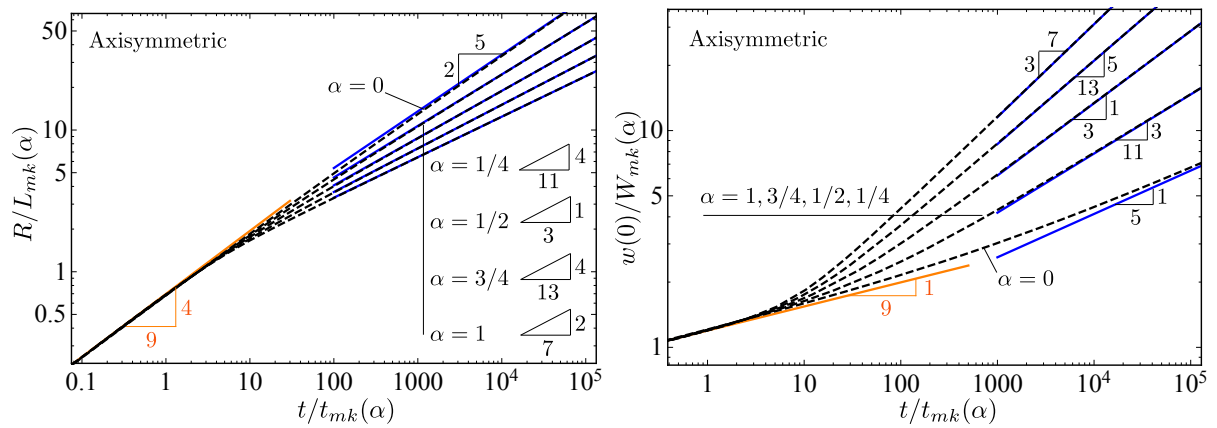

Fig. 5: Evolution of the dimensionless fracture radius (left) and inlet opening (right) with dimensionless time for a radial fracture. Dashed lines indicate the numerical simulations while the blue solid lines indicate the fracture length dependent zero-viscosity solutions and orange solid lines the zero-toughness solution.
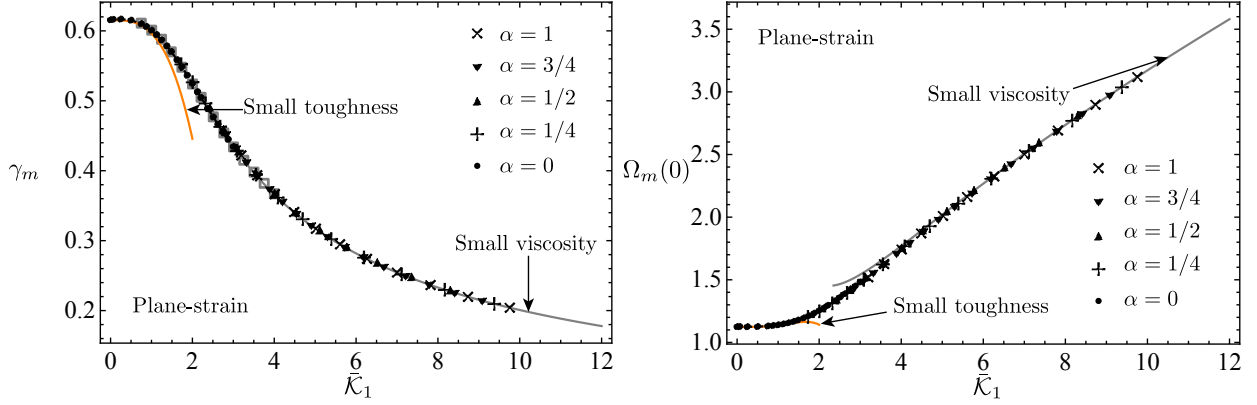
24

Fig. 6: Dependence of the dimensionless half-length γ_m (left) and inlet opening Ω_m (right) in the viscosity scaling on the scale-related dimensionless toughness $\bar{\mathcal{K}}_1$. Numerical solutions of $\alpha = 1/4, 1/2, 3/4, 1$ approximately coincide with the small-toughness [58] and small-viscosity [59] solutions ($\alpha = 0$) with first-order corrections, the previous numerical results (gray empty squares) [58] as well as the self-similar solutions (disks) calculated via the procedures in Appendix A.

current fracture length i.e.:

- Plane-strain ($d = 1$)

$$\bar{\mathcal{K}}_1 = \frac{K'_*}{E'} \left(\frac{E'}{\mu' Q_o} \right)^{1/4} \left(\frac{\ell}{\ell_*} \right)^{\alpha} \tag{57}$$

- Axisymmetric ($d = 2$)

$$\bar{\mathcal{K}}_2 = \frac{K'_*}{E'} \left(\frac{E'^5 t^2}{\mu'^5 Q_o^3} \right)^{1/18} \left(\frac{\ell}{\ell_*} \right)^{\alpha} \tag{58}$$

Such a definition explicitly embeds the fracture length dependence of the fracture toughness in the same dimensionless parameter as the fracture length independent toughness case [60]. After doing so, the dimensionless solution for any value of α expressed as function of $\bar{\mathcal{K}}_d$ approximately collapses on the same curve as the solution for fracture length independent toughness - see Figs 6, 7 for the dimensionless length and inlet opening. Fig. 8 presents the relative difference of the dimensionless length between the fracture length dependent and fracture length independent cases. The difference is null in both viscosity ($\bar{\mathcal{K}}_d = 0$) and toughness dominated ($\bar{\mathcal{K}}_d \to \infty$) regimes. Both end-member regimes are described by the fracture length independent solution with instantaneous value of toughness exactly, e.g. at large time, from Eq. (23), Eq. (24) and Eq. (17), the
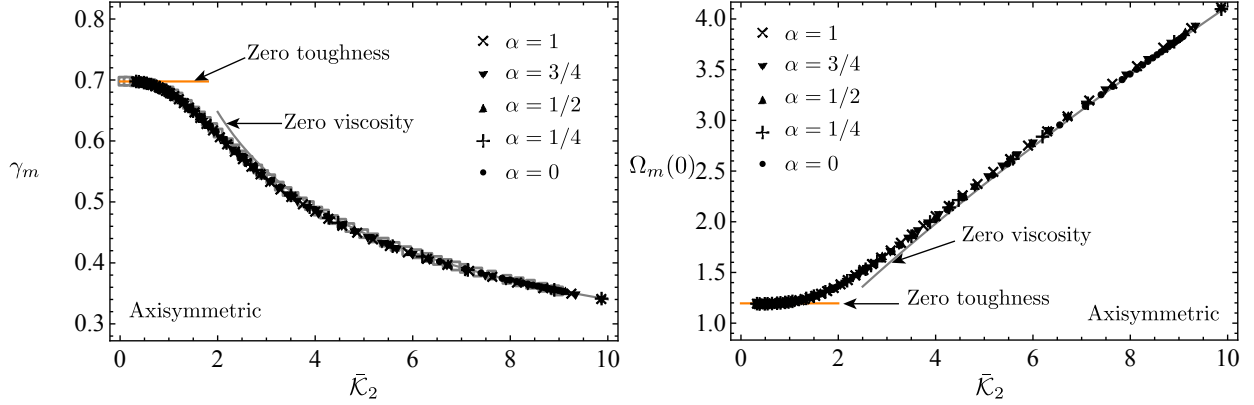
25

Fig. 7: Dependence of the dimensionless fracture radius γ_m (left) and inlet opening Ω_m (right) in the viscosity scaling on the scale-related dimensionless toughness $\bar{\mathcal{K}}_2$. Numerical solutions of $\alpha = 1/4, 1/2, 3/4, 1$ approximately coincide with the fracture length independent toughness solution ($\alpha = 0$) and the previous numerical solutions (gray empty squares) reported in [66] for the case of a fracture length independent toughness.

evolution of dimensionless fracture length with $\bar{\mathcal{K}}_d$ becomes independent of α:

$$\text{Plane-strain, } \gamma_m \approx \left(\frac{2\sqrt{2}}{\pi\bar{\mathcal{K}}_1}\right)^{2/3}; \quad \text{Axisymmetric, } \gamma_m \approx \left(\frac{3}{\pi\sqrt{2}\bar{\mathcal{K}}_2}\right)^{2/5} \tag{59}$$

The relative difference in the transient regime is not zero but remains very small with a maximum value of less than 2% as illustrated in Fig. 8.

For $\alpha \in [0,1]$, the change of apparent toughness has therefore a nearly instantaneous impact on the propagation of a plane-strain or axisymmetric fracture. The propagation of a hydraulic fracture can be therefore approximately dominated by one master curve, no matter how the apparent fracture toughness evolves in different scales and all solutions can be obtained from the fracture length independent toughness solution. It indicates that the solution obtained here numerically could be obtained from the fracture length independent toughness solution and a non-linear root finding scheme to determine the current length embedded in the definition of $\bar{\mathcal{K}}_d$.

7. Discussions

7.1. Emplacement scaling

The displacement to length or emplacement scaling is often used in geology to discuss the physics of the fracture propagation of magmatic dikes and natural fractures. Field observations of

26
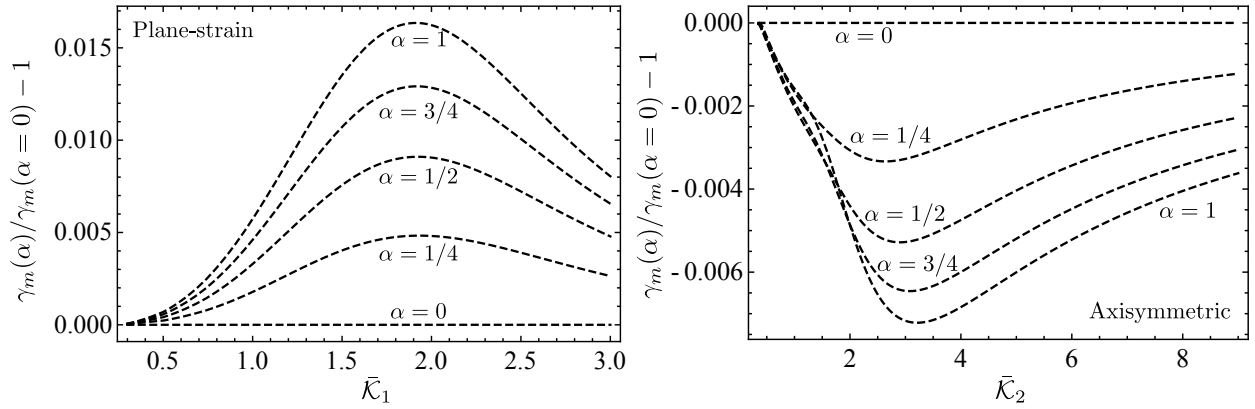
Fig. 8: Evolution of the relative difference of the dimensionless fracture length/radius γ_m (between the fracture length independent and fracture length dependent cases) with the instantaneous dimensionless toughness $\bar{\mathcal{K}}_d$. At the same value of $\bar{\mathcal{K}}_d$, a non-zero α results in a shorter fracture radius in the axisymmetric geometry, but a longer fracture length in the plane-strain geometry than the case of $\alpha = 0$ (fracture length independent). Such a discrepancy of a plane-strain fracture is due to the fact that $\bar{\mathcal{K}}_d(\alpha = 0)$ stays constant during the fracture growth instead of increasing as in the case of a radial fracture. For $\alpha > 0$, in order to reach the same value of $\bar{\mathcal{K}}_1(> \mathcal{K})$ for a plane-strain fracture in the fracture length dependent and -independent cases, the fracture toughness increases in the fracture length dependent cases before reaching such value of $\bar{\mathcal{K}}_1(> \mathcal{K})$. During this period of toughness increase, the instantaneous fracture toughness in the fracture length dependent case is smaller than that of the fracture length independent case, therefore indicates less energy dissipation in the creation of fracture surfaces and a longer fracture length.

displacement-length scaling have nourished discussions about the fracture length dependence of fracture toughness [31, 35]. In this section, we discuss the obtained displacement-length scaling for axisymmetric and plane-strain geometries for the power-law fracture length dependent toughness model.

The dimensional analysis reveals that both fracture opening and fracture length evolve with time and are related to the propagation regime associated with the principal source of energy dissipation. From Table 2, we obtain

$$M - \text{regime}, \quad W \propto L^{(3-d)/4}; \quad K - \text{regime}, \quad W \propto L^{\alpha+1/2} \tag{60}$$

At early time, when the fracture toughness has a negligible influence, the emplacement scaling is only geometry-dependent. At large time, for toughness dominated fractures, the emplacement scaling becomes independent of the geometry and is solely function of α: the larger α is, the larger the emplacement scaling W/L.

Fig. 9 illustrates the complete evolution of the emplacement scaling from the early time $M-$regime to the large time $K-$regime. For a plane-strain fracture with fracture length independent toughness, the scaling parameter happens to remain the same in all propagation regimes. For a fracture length dependent fracture toughness, the emplacement scaling increases from a lower value in the $M-$regime to a geometry-independent value in the $K-$regime at large time in both geometries. The displacement-length ratio reflects the evolution of the partitioning of energy between viscous flow and the creation of fracture surfaces during propagation.

A square-root emplacement scaling corresponds to the fracture length independent toughness as reported in the literature [21, 32, 33]. The linear emplacement scaling $W \propto L$ reported from field studies [31] corresponds to the case of a square-root fracture length dependent toughness ($\alpha = 1/2$). It is therefore interesting that, although debate exists in regards to the emplacement scaling observed in the field (either $1/2$ or linear), emplacement scaling ratio larger than one have not been reported. This seems to indicate that a power-law exponent larger than $\alpha = 1/2$ for the fracture length dependent toughness is unlikely.
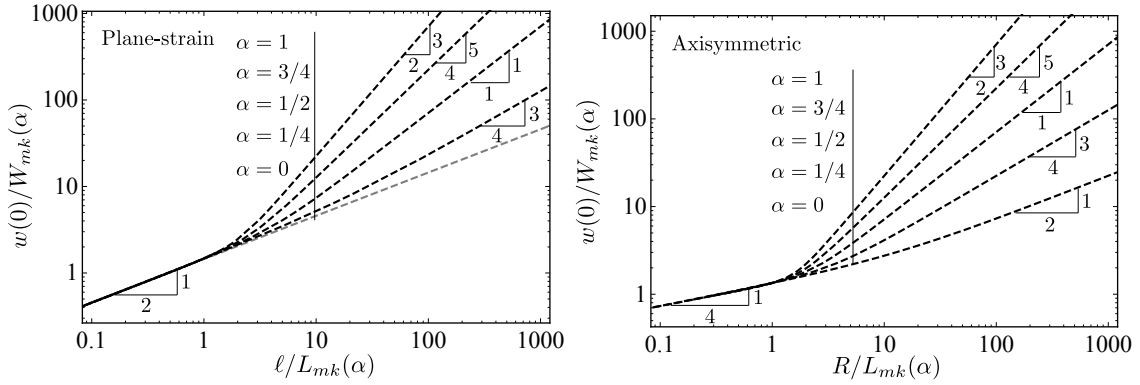
28

Fig. 9: Evolution of displacement-length scaling in two geometries: plane-strain (left) and axisymmetric (right) for different α values, scaled respectively by W_{mk} and L_{mk}.

7.2. Difference brought by the fracture length dependent toughness

The apparent fracture toughness may exhibit a lower cut-off K_c within a cross-over length scale ℓ_c. For most quasi-brittle materials, ℓ_c is of the same order of magnitude as specimen dimensions in the lab. In order to grasp the difference brought by an increasing toughness, it is natural to choose a reference state corresponding to a fracture toughness $K_* \approx K_c$ measured at a laboratory length scale $\ell_* \approx \ell_c$. In this section, we analyse the difference brought by the power-law dependence compared with the fracture length independent case assuming $\ell_s \to \infty$.

When $\ell \leq \ell_*$, the fracture energy reduces to a constant and does not vary with the fracture length. The growth of hydraulic fractures is the same as the case of the fracture length independent toughness with $K_{Ic} = K_*$. We define t_* as the time for the fracture to propagate with a constant toughness K_* in order to reach a fracture length of ℓ_*. When $\ell > \ell_*$, the apparent toughness scales with the fracture length and the propagation transitions to large toughness solutions as discussed in Section 6. The ratio between the large toughness solutions of the fracture length dependent and independent cases are shown in Table 3, where the corresponding power laws can be recovered at large time by the numerical solutions as illustrated in Figs 10 and 11. The evolution of the difference ratio depends strongly on the reference state where the apparent toughness starts to scale with the fracture length. Such a reference state can be characterised by $\ell_*/L_{mk}(\alpha = 0)$ for a radial fracture and by $\mathcal{K}(\ell = \ell_*, \alpha = 0)$ for a plane-strain fracture. As shown in Fig. 10, a transition of principal energy dissipation from viscosity to toughness appears if the viscosity happens to

29

Table 3: Time dependence of the difference ratio between the large toughness solutions for fracture length dependent toughness and fracture length independent toughness, respectively. Such difference ratios of inlet opening, net pressure and fracture length scale are power laws of the dimensionless time $(t/t_{mk}(\alpha = 0))^\beta$ for an axisymmetric fracture and $(t/t_*)^\beta$ for a plane-strain fracture, with the exponent β a function of the geometry index d and toughness power-law scaling exponent α.

Geometry	Time power-law exponent β	
	Plane-strain ($d = 1$)	Axisymmetric ($d = 2$)
$w(0,\alpha)/w(0,\alpha = 0)$	$2\alpha/(3\alpha + 9/2)$	$4\alpha/(5\alpha + 25/2)$
$p(0,\alpha)/p(0,\alpha = 0)$	$4\alpha/(3\alpha + 9/2)$	$6\alpha/(5\alpha + 25/2)$
$\ell(\alpha)/\ell(\alpha = 0)$	$-2\alpha/(3\alpha + 9/2)$	$-2\alpha/(5\alpha + 25/2)$

dominate the fracture growth at the reference state. Both a smaller length scale for the initiation of the toughening effect and a larger value of the power-law exponent α result in a more pronounced difference as illustrated in Fig. 10 and Fig. 11.

Using values for material and injection parameters - representative of an industrial fracturing treatment, we quantify the departure of the solution from the fracture length independent toughness case for a radial fracture in Table 4. The characteristic net pressure increases with α while the characteristic length, as well as, the characteristic transition time from the viscosity to the toughness dominated regime, decreases with α. The relative difference of the fracture radius can go up to 40% after long injection duration for $\alpha = 1/2$.

7.3. Effect of a finite apparent fracture toughness beyond a given length scale

The fracture toughness might reach an asymptotic value beyond a certain length scale ℓ_s, possibly due to the saturation of the process zone size or the limits of the constraints of the medium dimensions (earth crust). In this section, we model such possible saturation of the fracture toughness ($\ell_s < \infty$) as follows:

$$K_{Ic} = K_* (\ell/\ell_*)^\alpha (1 - f((\ell - \ell_s)/\ell_*)) + K_s f((\ell - \ell_s)/\ell_*), \quad K_s = K_* (\ell_s/\ell_*)^\alpha \qquad (61)$$

Here f is a smoothed Heaviside step function $f(m) = 1/(1 + \exp(-2hm))$, where h is a positive dimensionless number controlling the smoothing of the approximation (a smaller value entails a
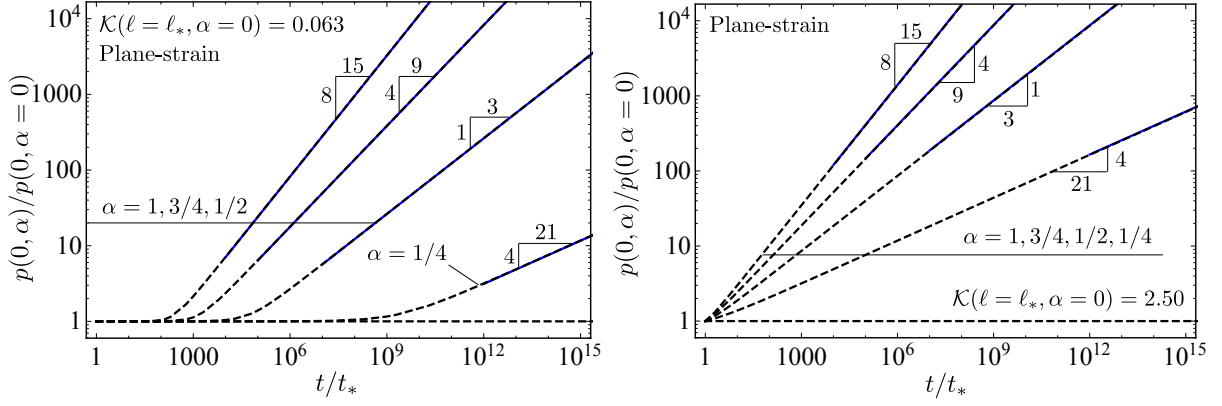
30

Fig. 10: Evolution of the difference ratio of net pressure at the inlet with dimensionless time in a plane-strain fracture for $\mathcal{K}(\ell = \ell_*, \alpha = 0) = 0.063$ (left), 2.50 (right), dashed lines indicate the numerical simulations while the blue solid lines indicate the fracture length dependent zero-viscosity solutions.
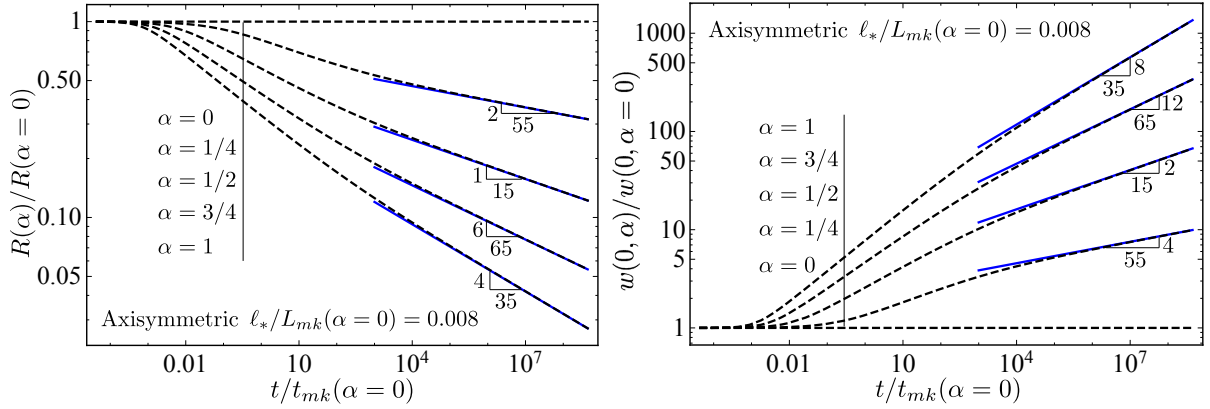

Fig. 11: Evolution of the difference ratio of fracture radius (left) and inlet opening (right) with dimensionless time in a radial fracture ($\ell_*/L_{mk}(\alpha = 0) = 0.008$), dashed lines indicate the numerical simulations while the blue solid lines indicate the fracture length dependent zero-viscosity solutions.

31

Table 4: Characteristic scales and difference ratio values for different values of the toughness power-law scaling exponent α in the axisymmetric geometry ($E' = 20\,\text{GPa}$, $Q_o = 2 \times 10^{-2}\,\text{m}^3/\text{s}$, $\mu' = 3\,\text{Pa.s}$, $K_* = 1.5\,\text{MPa.m}^{1/2}$, $\ell_* = 0.1\,\text{m}$ and $\ell_*/L_{mk}(\alpha = 0) = 1.03 \times 10^{-8}$)

	$\alpha = 0$	$\alpha = 1/4$	$\alpha = 1/2$
$t_{mk}(\alpha)$ (s)	3.56×10^{14}	3.67×10^5	3.70×10^2
$L_{mk}(\alpha)$ (m)	9.84×10^6	9.97×10^2	46.5
$P_{mk}(\alpha)$ (kPa)	0.150	1.48×10^2	1.48×10^3
$R/R(\alpha = 0)$ ($t = 90$ min)	1	1.00	0.88
$w(0)/w(\alpha = 0)$ ($t = 90$ min)	1	1.00	1.14
$R/R(\alpha = 0)$ ($t = 3$ d)	1	0.98	0.60
$w(0)/w(\alpha = 0)$ ($t = 3$ d)	1	1.01	2.26

$_{529}$ "smoother step" - we have used $h = 130$ here). Under the same assumption that $\ell_* \approx \ell_c$ as in

$_{530}$ Section 7.2, the saturation length scale is comparable to or larger than the reference length scale:

$_{531}$ $\ell_s \geq \ell_*$. $(\ell_s/\ell_*)^\alpha$ therefore describes the difference of apparent toughness between the reference

$_{532}$ and final state whereas α characterises the slope of the power law branch. When $\ell_s \gg \ell_*$, the

$_{533}$ saturated apparent toughness K_s can be exceedingly large compared to K_*.

$_{534}$ As illustrated in Fig. 12 (for $\alpha = 1/2$ and different values of $\ell_s/L_{mk}(\alpha)$), the hydraulic frac-

$_{535}$ ture evolves by first following the solution obtained previously for the power-law fracture length

$_{536}$ dependent toughness and then transitions back to the fracture length independent toughness so-

$_{537}$ lution ($\alpha = 0$ with $K_{Ic} = K_s$) when the fracture reaches the saturation length scale $\ell = \ell_s$. The

$_{538}$ impact of the toughness evolution on fracture growth is nearly instantaneous for $\alpha \in [0, 1]$ in both

$_{539}$ geometries as previously shown in Figs. 6 and 7, however, the transition towards the toughness

$_{540}$ dominated solution at large timescale with a fracture length independent toughness ($\alpha = 0$ with

$_{541}$ $K_{Ic} = K_s$) can be much more gradual for a radial fracture when $\ell_s/L_{mk}(\alpha) \ll 1$ in Fig. 12.

$_{542}$ The effect of the toughness saturation on the propagation of a hydraulic fracture with fracture

$_{543}$ length dependent toughness up to ℓ_s can be summarized in the propagation diagram of Fig. 13.

$_{544}$ A plane-strain hydraulic fracture evolves initially from the reference state which can be either

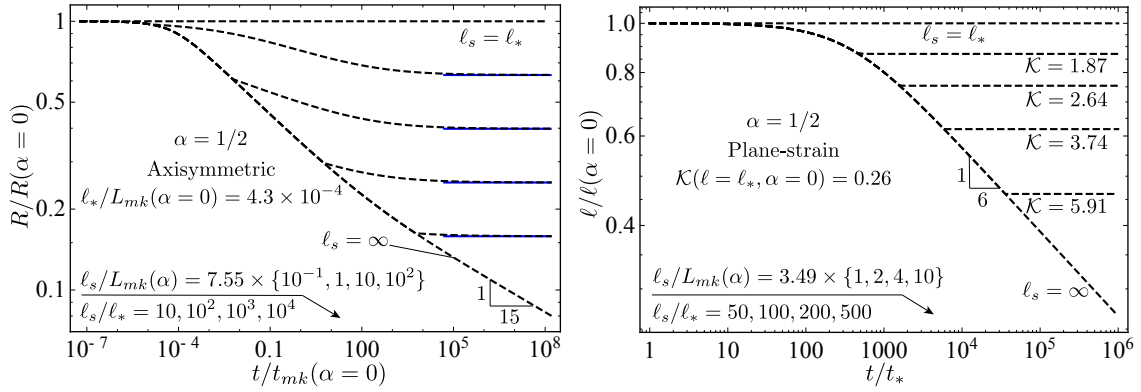$_{545}$ viscosity or toughness dominated towards the fracture length dependent toughness edge ($M - K_\alpha$)

Fig. 12: Evolution of the difference ratio of dimensionless fracture radius (left) and fracture half-length (right) with dimensionless time where $\alpha = 1/2$. Dashed curves indicate the numerical transition and blue solid lines refer to zero-viscosity solutions.
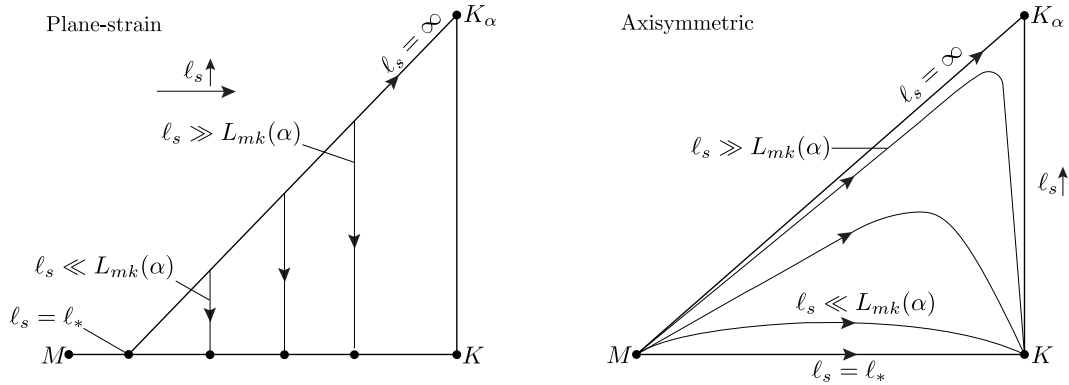

Fig. 13: Propagation diagram illustrating the propagation of a hydraulic fracture in a material exhibiting a fracture length dependent toughness with a saturated length scale ℓ_s for plane-strain and axisymmetric geometries. K_α signifies the fracture length dependent toughness dominated regime.

546 (see Fig. 13-left), and, as soon as the fracture half-length ℓ reaches ℓ_s, the propagation switches

547 to the fracture length independent toughness, plane-strain self-similar solution characterised by a

548 constant dimensionless toughness $\bar{\mathcal{K}}_1(\ell = \ell_s)$ from Eq. (57). Depending on the value of $\bar{\mathcal{K}}_1(\ell = \ell_s)$,

549 any state between the $M-$ and $K-$regime is possible at large time for a plane-strain hydraulic

550 fracture. The effect of toughness saturation for the radial hydraulic fracture is similar pending the

551 fact that due to the geometry, the propagation always ends up being toughness dominated at large

552 time - with the final toughness K_s governing the characteristic scales (see Fig. 13-right).

8. Conclusions

554 We have investigated theoretically the growth of a plane-strain and axisymmetric hydraulic

555 fracture, assuming a power-law dependence of the fracture toughness with fracture length $K_{Ic} \propto \ell^\alpha$.

556 We have posed the hydraulic fracture propagation problem based on the usual assumptions of

557 linear elastic fracture mechanics, assuming that the small scale yielding approximation remains

558 always valid and that the fracture is much larger than the process zone size.

559 In order to solve such a HF problem, we have developed a highly efficient and accurate numeri-

560 cal scheme based on the combination of Gauss-Chebyshev quadrature with barycentric differentia-

561 tion and interpolation. Using such a spatial discretization allows to recast the non-linear, non-local

562 hydraulic fracture evolution problem into a system of non-linear ordinary differential equations

563 (ODEs) that can be solved by existing ODE integration schemes. The scheme performs extremely

564 well against the published hydraulic fracture growth solutions for constant fracture toughness.

565 Our numerical results quantify precisely the impact of a power-law fracture length dependent

566 toughness on HF growth. The increase of fracture energy with fracture length yields shorter and

567 wider hydraulic fracture, and larger net fluid pressure. Our results demonstrate a shortening of

568 the viscosity dominated to toughness dominated propagation for a radial fracture and show the

569 existence of a viscosity to-toughness transition for a plane-strain fracture, a transition which does

570 not exist in the case of a constant fracture toughness. The hydraulic fracture growth with a power-

571 law toughness can be always very accurately approximated by the constant toughness solution

572 when using the instantaneous value of toughness (function of the current fracture length), as per

573 Eq. (57) and Eq. (58). If the fracture toughness saturates beyond a given scale ℓ_s, the hydraulic

34

fracture propagation transitions back to the constant toughness solution as soon as $\ell > \ell_s$ - as depicted in Fig. 12.

Our results obviously depend on the value of the power-law scaling exponent α, with large changes between $\alpha \leq 1/2$ and $\alpha > 1/2$. The predicted emplacement scaling (ratio of displacement to length) is geometry-dependent in the viscosity dominated regime: $W \propto L^{1/2}$ for plane-strain, $W \propto L^{1/4}$ for axisymmetric geometry. It is however solely dependent on α in the toughness dominated regime with $W \propto L^{1/2+\alpha}$. Compared to these theoretical predictions, emplacement W/L observations of dikes tend to indicate that the power-law scaling exponent α should at most be equal to $1/2$ [31]. Such a limit appears consistent with available experimental evidences (Table 1) pointing to values of α lower than $1/2$.

More field and experimental studies are needed in order to better quantify the importance of a possible fracture length dependence of fracture energy in relation to industrial as well as natural hydraulic fractures. The scalings and numerical results derived here could help decipher the validity of the power-law dependence hypothesis of apparent fracture toughness and guide further investigations.

Acknowledgement

Appendix A. Discretization for the plane-strain self-similar problem

For a plane-strain hydraulic fracture, the dimensionless toughness $\mathcal{K}$ determines the solution of the self-similar problem. We rewrite the dimensionless governing equations in the viscosity scaling by introducing a new dimensionless opening [58].

$$\bar{\Omega} = \Omega/\gamma \tag{A.1}$$

The governing equations becomes:

- Elasticity

$$4\Pi = \frac{1}{\pi} \int_{-1}^{+1} \frac{\partial \bar{\Omega}}{\partial \xi'} G_1(\xi, \xi') \mathrm{d}\xi' \tag{A.2}$$

- Lubrication flow

$$\int_{\xi}^{1} \frac{\partial \bar{\Omega}}{\partial \xi} \mathrm{d}\xi + \frac{2}{3}\xi\bar{\Omega} + \bar{\Omega}^3 \frac{\mathrm{d}\Pi}{\mathrm{d}\xi} = 0 \tag{A.3}$$

- Global continuity equation

$$\int_{-1}^{1} \bar{\Omega} \mathrm{d}\xi = \frac{1}{\gamma^2} \tag{A.4}$$

- Propagation criterion

$$\bar{\Omega} \sim \frac{\mathcal{K}}{\sqrt{\gamma}}(1 - \xi)^{1/2} \tag{A.5}$$

We select the Gauss-Chebyshev polynomials of the first type T_n for discretization.

$$\frac{\partial \bar{\Omega}}{\partial s} = \omega(s)F(s), \quad \omega(s) = \frac{1}{\sqrt{1 - s^2}} \tag{A.6}$$

The discretized equations reduce to

$$4\mathbf{\Pi} = \mathbb{G}_1 \cdot \mathbf{F} \tag{A.7}$$

$$-\mathbf{z}(\mathbb{S} \cdot \mathbf{F}) + \mathbb{S} \cdot (\mathbf{s}\,\mathbf{F}) + \frac{2}{3}\mathbf{z}(\mathbb{S} \cdot \mathbf{F}) + (\mathbb{S} \cdot \mathbf{F})^3(\mathbb{D} \cdot \mathbf{\Pi}) = 0 \tag{A.8}$$

$$\mathbf{S}_A \cdot (\mathbf{s}\,\mathbf{F}) + \frac{1}{\gamma^2} = 0 \tag{A.9}$$

$$\mathbf{Q} \cdot \mathbf{F} + \frac{1}{\sqrt{2}}\frac{\mathcal{K}}{\sqrt{\gamma}} = 0 \tag{A.10}$$

By back-substituting the elasticity (A.7) into the lubrication equations (A.8), we get $(n + 1)$ equations including the global continuity (A.9) and the propagation criterion (A.10). On the account of the problem symmetry as in Eq. (55), the first $(n/2-1)$ equations of Eq. (48) are equivalent to the last $(n/2 - 1)$ equations. We hence account for the first $(n/2 - 1)$ equations of Eq. (A.8) together with Eq. (A.9) and (A.10) and solve the solutions of $\{\gamma, \mathbf{F}\}$ using the Mathematica built-in function *FindRoot*. As illustrated in Fig. 6, the numerical results fit well the small-toughness and small-viscosity solutions [58, 59], and also the previous numerical solutions [58].

References

[1] B. Lecampion, J. Desroches, R. G. Jeffrey, A. P. Bunger, Experiments versus theory for the initiation and propagation of radial hydraulic fractures in low-permeability materials, Journal of Geophysical Research: Solid Earth 122 (2) (2017) 1239–1263.

[2] P. Xing, K. Yoshioka, J. Adachi, A. El-Fayoumi, A. P. Bunger, Laboratory measurement of tip and global behavior for zero-toughness hydraulic fractures with circular and blade-shaped (pkn) geometry, Journal of the Mechanics and Physics of Solids 104 (2017) 172–186.

[3] A. P. Bunger, E. Detournay, Experimental validation of the tip asymptotics for a fluid-driven crack, Journal of the Mechanics and Physics of Solids 56 (11) (2008) 3101–3115.

[4] D. I. Garagash, Scaling of physical processes in fluid-driven fracture: perspective from the tip, in: IUTAM symposium on scaling in solid mechanics, Springer, 2009, pp. 91–100.

[5] E. Detournay, Mechanics of hydraulic fractures, Annual Review of Fluid Mechanics 48 (2016) 311–339.

[6] J. Shlyapobersky, M. A. Issa, M. A. Issa, M. Islam, J. W. Dudley, Y. Shulkin, A. Chudnovsky, Scale effects on fracture growth resistance in poroelastic materials, in: SPE Annual Technical Conference and Exhibition, SPE, Orleans, Louisiana, 1998, pp. 29–38.

[7] J. Shlyapobersky, Energy analysis of hydraulic fracturing, in: The 26th US Symposium on Rock Mechanics (USRMS), ARMA, Rapid City, South Dakota, 1985.

[8] J. Shlyapobersky, G. Wong, W. Walhaug, Overpressure calibrated design of hydraulic fracture stimulations, in: SPE Annual Technical Conference and Exhibition, SPE, 1988, pp. 133–148.

[9] S. Thallak, J. Holder, K. Gray, The pressure dependence of apparent hydrofracture toughness, in: The 34th US Symposium on Rock Mechanics (USRMS), ARMA, Madison, Wisconsin, 1993.

[10] I. D. Palmer, R. W. Veatch Jr, Abnormally high fracturing pressures in step-rate tests, SPE Production Engineering 5 (03) (1990) 315–323.

[11] A. Bunger, B. Lecampion, Four critical issues for successful hydraulic fracturing applications, no. Chapter 16, CRC Press, 2017.

[12] A. M. Rubin, Tensile fracture of rock at high confining pressure: implications for dike propagation, Journal of Geophysical Research: Solid Earth 98 (B9) (1993) 15919–15935.

[13] P. Papanastasiou, The effective fracture toughness in hydraulic fracturing, International Journal of Fracture 96 (2) (1999) 127–147.

[14] P. Papanastasiou, M. Thiercelin, Influence of inelastic rock behaviour in hydraulic fracturing, in: International journal of rock mechanics and mining sciences & geomechanics abstracts, Vol. 30, Elsevier, 1993, pp. 1241–1247.

[15] P. Papanastasiou, The influence of plasticity in hydraulic fracturing, International Journal of Fracture 84 (1) (1997) 61–79.

37

[16] P. Papanastasiou, C. Atkinson, Representation of crack-tip plasticity in pressure sensitive geomaterials: Large scale yielding, International Journal of Fracture 139 (1) (2006) 137–144.

[17] E. Sarris, P. Papanastasiou, Numerical modeling of fluid-driven fractures in cohesive poroelastoplastic continuum, International Journal for Numerical and Analytical Methods in Geomechanics 37 (12) (2013) 1822–1846.

[18] T. Hashida, K. Sato, H. Takahashi, Significance of crack opening for determining the growth behavior monitoring of hydrofractures, in: Eighteenth Workshop on Geothermal Reservoir Engineering, Stanford, California, 1993, pp. 79–84.

[19] D. B. van Dam, The influence of inelastic rock behaviour on hydraulic fracture geometry, Ph.D. thesis, TU Delft, Delft University of Technology (1999).

[20] E. Rivalta, B. Taisne, A. Bunger, R. Katz, A review of mechanical models of dike propagation: Schools of thought, results and future directions, Tectonophysics 638 (2015) 1–42.

[21] J. E. Olson, Sublinear scaling of fracture aperture versus length: An exception or the rule?, Journal of Geophysical Research: Solid Earth 108 (B9) (2003) 2413.

[22] P. T. Delaney, D. D. Pollard, Deformation of host rocks and flow of magma during growth of minette dikes and breccia-bearing intrusions near ship rock, New Mexico, Tech. rep., USGPO (1981).

[23] Z.-H. Jin, S. E. Johnson, Magma-driven multiple dike propagation and fracture toughness of crustal rocks, Journal of Geophysical Research: Solid Earth 113 (2008) B03206.

[24] E. Rivalta, T. Dahm, Acceleration of buoyancy-driven fractures and magmatic dikes beneath the free surface, Geophysical Journal International 166 (3) (2006) 1424–1439.

[25] A. Bunger, A. Cruden, Modeling the growth of laccoliths and large mafic sills: Role of magma body forces, Journal of Geophysical Research 116 (2011) B02203.

[26] B. K. Atkinson, Subcritical crack growth in geological materials, Journal of Geophysical Research: Solid Earth 89 (B6) (1984) 4077–4114.

[27] B. K. Atkinson, P. G. Meredith, Experimental fracture mechanics data for rocks and minerals, Fracture mechanics of rock (1987) 477.

[28] P. T. Delaney, D. D. Pollard, J. I. Ziony, E. H. McKee, Field relations between dikes and joints: Emplacement processes and paleostress analysis, Journal of Geophysical Research: Solid Earth 91 (B5) (1986) 4920–4938.

[29] D. D. Pollard, Theoretical displacements and stresses near fractures in rock: with applications to faults, joints, veins, dikes, and solution surfaces, Fracture mechanics of rock (1987) 277–349.

[30] A. K. Engvik, A. Bertram, J. F. Kalthoff, B. Stöckhert, H. Austrheim, S. Elvevold, Magma-driven hydraulic fracturing and infiltration of fluids into the damaged host rock, an example from Dronning Maud Land, Antarctica, Journal of Structural Geology 27 (5) (2005) 839–854.

[31] C. H. Scholz, A note on the scaling relations for opening mode fractures in rock, Journal of Structural Geology 32 (10) (2010) 1485–1487.

[32] R. A. Schultz, R. Soliva, H. Fossen, C. H. Okubo, D. M. Reeves, Dependence of displacement–length scaling relations for fractures and deformation bands on the volumetric changes across them, Journal of Structural Geology 30 (11) (2008) 1405–1411.

[33] R. A. Schultz, D. Mège, H. Diot, Emplacement conditions of igneous dikes in ethiopian traps, Journal of Volcanology and Geothermal Research 178 (4) (2008) 683–692.

[34] P. A. Cowie, C. H. Scholz, Physical explanation for the displacement-length relationship of faults using a post-yield fracture mechanics model, Journal of Structural Geology 14 (10) (1992) 1133–1148.

[35] J. E. Olson, R. A. Schultz, Comment on "A note on the scaling relations for opening mode fractures in rock" by C.H. Scholz, Journal of Structural Geology 33 (10) (2011) 1523–1524.

[36] A. P. Bunger, A rigorous tool for evaluating the importance of viscous dissipation in sill formation: it's in the tip, Geological Society, London, Special Publications 304 (1) (2008) 71–81.

[37] T. Funatsu, M. Seto, H. Shimada, K. Matsui, M. Kuruppu, Combined effects of increasing temperature and confining pressure on the fracture toughness of clay bearing rocks, International Journal of Rock Mechanics and Mining Sciences 41 (6) (2004) 927–938.

[38] D. I. Garagash, Roughness-dominated hydraulic fracture propagation, in: 2015 AGU Fall Meeting Abstracts, AGU, San Francisco, 2015.

[39] T. L. Anderson, Fracture mechanics: fundamentals and applications, 4th Edition, CRC press, Boca Raton, 2017.

[40] J. Dempsey, R. Adamson, S. Mulmule, Scale effects on the in-situ tensile strength and fracture of ice. part ii: First-year sea ice at resolute, nwt, International Journal of Fracture 95 (1-4) (1999) 347.

[41] S. Morel, E. Bouchaud, J. Schmittbuhl, G. Valentin, R-curve behavior and roughness development of fracture surfaces, International Journal of Fracture 114 (4) (2002) 307–325.

[42] J. R. Rice, Mathematical analysis in the mechanics of fracture, Fracture: an advanced treatise 2 (1968) 191–311.

[43] P. Papanastasiou, C. Atkinson, et al., The brittleness index in hydraulic fracturing, in: 49th US Rock Mechanics /Geomechanics Symposium, ARMA, 2015.

[44] P. Papanastasiou, C. Atkinson, Representation of crack-tip plasticity in pressure sensitive geomaterials, International Journal of Fracture 102 (3) (2000) 271–286.

[45] P. Papanastasiou, E. Papamichos, C. Atkinson, On the risk of hydraulic fracturing in CO2 geological storage, International Journal for Numerical and Analytical Methods in Geomechanics 40 (10) (2016) 1472–1484.

[46] J. M. López, J. Schmittbuhl, Anomalous scaling of fracture surfaces, Physical Review E 57 (6) (1998) 6405.

[47] G. Mourot, S. Morel, E. Bouchaud, G. Valentin, Scaling properties of mortar fracture surfaces, International Journal of Fracture 140 (1-4) (2006) 39–54.

[48] R. Weisinger, L. Costin, T. Lutz, K_{Ic} and J-resistance-curve measurements on Nevada tuff, Experiemntal Mechanics 20 (2) (1980) 68–72.

[49] R. C. Viesca, D. I. Garagash, Numerical methods for coupled fracture problems, Journal of the Mechanics and

Physics of Solids 113 (2018) 13–34.

[50] A. Savitski, E. Detournay, Propagation of a penny-shaped fluid-driven fracture in an impermeable rock: asymptotic solutions, International Journal of Solids and Structures 39 (26) (2002) 6311–6337.

[51] E. Detournay, Propagation regimes of fluid-driven fractures in impermeable rocks, International Journal of Geomechanics 4 (1) (2004) 35–45.

[52] D. A. Hills, P. Kelly, D. Dai, A. Korsunsky, Solution of crack problems: the distributed dislocation technique, Vol. 44, Springer Science & Business Media, 2013.

[53] M. Cleary, S. Wong, Numerical simulation of unsteady fluid flow and propagation of a circular hydraulic fracture, International Journal for Numerical Analytical Methods in Geomechanics 9 (1) (1985) 1–14.

[54] E. Gordeliy, E. Detournay, Displacement discontinuity method for modeling axisymmetric cracks in an elastic half-space, International Journal of Solids and Structures 48 (19) (2011) 2614–2629.

[55] B. Lecampion, A. Bunger, X. Zhang, Numerical methods for hydraulic fracture propagation: a review of recent trends, Journal of Natural gas Science and Engineering 49 (2018) 66–83.

[56] G. K. Batchelor, An introduction to fluid dynamics, Cambridge University Press, 2000.

[57] E. Detournay, A. P. Peirce, On the moving boundary conditions for a hydraulic fracture, International Journal of Engineering Science 84 (2014) 147–155.

[58] D. I. Garagash, E. Detournay, Plane-strain propagation of a fluid-driven fracture: small toughness solution, ASME Journal of Applied Mechanics 72 (6) (2005) 916–928.

[59] D. I. Garagash, Plane-strain propagation of a fluid-driven fracture during injection and shut-in: Asymptotics of large toughness, Engineering Fracture Mechanics 73 (4) (2006) 456 – 481.

[60] D. I. Garagash, Hydraulic fracture propagation in elastic rock with large toughness, in: 4th North American Rock Mechanics Symposium, ARMA, Seattle, Washington, 2000, pp. 221–228.

[61] M. J. Economides, K. G. Nolte, et al., Reservoir stimulation, Vol. 2, Prentice Hall Englewood Cliffs, NJ, 1989.

[62] S. N. Gulrajani, K. G. Nolte, J. Romero, Evaluation of the M-Site B-Sand fracture experiments: The evolution of a pressure analysis methodology, in: SPE Annual Technical Conference and Exhibition, SPE, 1997.

[63] F. Erdogan, G. D. Gupta, T. Cook, Numerical solution of singular integral equations, in: Methods of analysis and solutions of crack problems, Springer, 1973, pp. 368–425.

[64] J. P. Berrut, L. N. Trefethen, Barycentric lagrange interpolation, SIAM Review 46 (3) (2004) 501–517.

[65] Wolfram Research, Inc., Mathematica, version 11.0 Edition, Wolfram Research, Inc., Champaign, Illinois, 2016.

[66] M. V. Madyarova, Fluid-driven penny-shaped fracture in elastic medium, Master's thesis, University of Minnesota (2003).